UC Berkeley

Title

Bidirectional Control of Autophagy by BECN1 BARA Domain Dynamics

Permalink

Journal

ISSN

Authors

Chang, Chunmei
Young, Lindsey N
Morris, Kyle L
et al.

Publication Date

2019

DOI

Peer reviewed

Bidirectional control of autophagy by BECN1 BARA domain dynamics

Chunmei Chang[1,†], **Lindsey N. Young**[2,†], **Kyle L. Morris**[1], **Sören von Bülow**[3], **Johannes Schöneberg**[1], **Hitomi Yamamoto-Imoto**[4], **Yukako Oe**[4], **Kentaro Yamamoto**[4], **Shuhei Nakamura**[4], **Goran Stjepanovic**[2], **Gerhard Hummer**[5], **Tamotsu Yoshimori**[4], and **James H. Hurley**[6,*]

[1]Department of Molecular and Cell Biology, University of California, Berkeley, Berkeley, CA 94720, USA; California Institute for Quantitative Biosciences, University of California, Berkeley, Berkeley, CA 94720, USA.

[2]Department of Molecular and Cell Biology, University of California, Berkeley, Berkeley, CA 94720, USA; California Institute for Quantitative Biosciences, University of California, Berkeley, Berkeley, CA 94720, USA; Molecular Biophysics and Integrated Bioimaging Division, Lawrence Berkeley National Laboratory, Berkeley, CA 94720, USA.

[3]Department of Theoretical Biophysics, Max Planck Institute of Biophysics, 60438 Frankfurt/M, Germany.

[4]Department of Genetics, Graduate School of Medicine, Osaka University, Osaka 565-0871, Japan.

[5]Department of Theoretical Biophysics, Max Planck Institute of Biophysics, 60438 Frankfurt/M, Germany; Institute of Biophysics, Goethe University, 60438 Frankfurt/M, Germany.

[6]Department of Molecular and Cell Biology, University of California, Berkeley, Berkeley, CA 94720, USA; California Institute for Quantitative Biosciences, University of California, Berkeley, Berkeley, CA 94720, USA; Molecular Biophysics and Integrated Bioimaging Division, Lawrence Berkeley National Laboratory, Berkeley, CA 94720, USA

Summary

*Lead Contact: James H. Hurley, jimhurley@berkeley.edu.
†These authors contributed equally.

Declaration of Interests
C.C., L.Y.N., J.H.H., and UC Berkeley have applied for patents for protein constructs and assays related to this work. J.H.H. is a founder of Casma Therapeutics.

Supplemental Information
Supplemental information includes six figures, one table and two movies.

Membrane targeting of the BECN1-containing class III PI 3-kinase (PI3KC3) complexes is pivotal to the regulation of autophagy. The interaction of PI3KC3 complex II and its ubiquitously expressed inhibitor, Rubicon, was mapped to the first β sheet of the BECN1 BARA domain and the UVRAG BARA2 domain by hydrogen-deuterium exchange and cryo-EM. These data suggested that BARA β sheet-1 unfolds to directly engage the membrane. This mechanism was confirmed using protein engineering, giant unilamellar vesicle assays, and molecular simulations. Using this mechanism, a BECN1 β sheet-1-derived peptide activates both PI3KC3 complexes I and II, while HIV-1 Nef inhibits complex II. These data reveal how BECN1 switches on and off PI3KC3 binding to membranes. The observations explain how PI3KC3 inhibition by Rubicon, activation by autophagy-inducing BECN1 peptides, and inhibition by HIV-1 Nef, are mediated by the switchable ability of the BECN1 BARA domain to partially unfold and insert into membranes.

eTOC Blub

A structural, biochemical, and biophysical study of PI 3-kinase regulation by Rubicon, HIV-1 Nef, and an autophagy activating peptide shows how BECN1 BARA domain is switched on and off in both physiology and infection, and how it can be targeted for therapeutic induction of autophagy.

Graphical Abstract
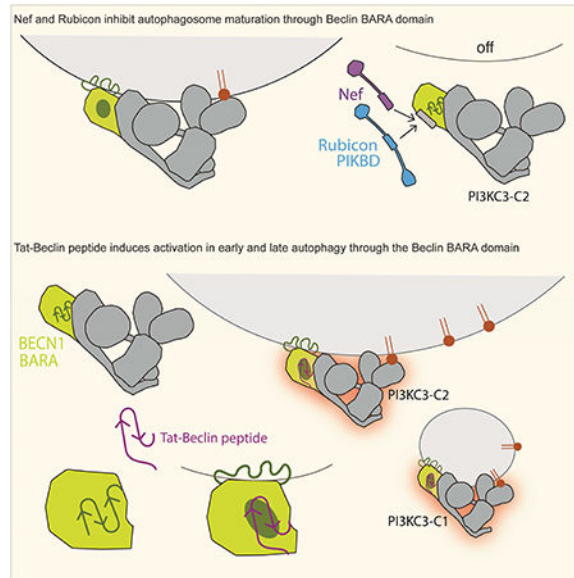
Autophagy is the degradative process of cytosolic cargo engulfment by the double membrane phagophore (also known as the isolation membrane) for its transport to the lysosome (Mizushima et al., 2011). Autophagy is essential for cellular homeostasis and survival during starvation. Autophagic dysfunction is thought to contribute to neurodegeneration, cancer, aging, infection, and liver and other diseases (Mizushima et al., 2008), and inducers of autophagy are actively being sought as candidate therapeutic agents (Galluzzi et al., 2017). The generation of phosphatidylinositol 3-phosphate (PI(3)P) by the class III phosphatidylinositol 3-kinase (PI3KC3) complexes I and II (PI3KC3-C1 and –C2) (Itakura et al., 2008; Itakura and Mizushima, 2009; Kihara et al., 2001; Sun et al., 2008) is

central to the initiation and expansion of the phagophore (Bento et al., 2016; Hurley and Young, 2017; Mercer et al., 2018).

All PI3KC3 complexes contain the lipid kinase VPS34, the scaffold and putative protein kinase VPS15, and the regulatory subunit BECN1 (Backer, 2016; Hurley and Young, 2017). PI3KC3-C1 and C2 are distinguished by the mutually exclusive presence of either ATG14 or UVRAG (Itakura et al., 2008; Liang et al., 2008; Matsunaga et al., 2009; Sun et al., 2008; Zhong et al., 2009), respectively, which both engage with the core complex via the central coiled-coil of BECN1 (Li et al., 2012). PI3KC3-C1 functions in autophagy initiation (Itakura et al., 2008; Obara et al., 2006; Sun et al., 2008), while PI3KC3-C2 functions in both in phagophore expansion (Itakura et al., 2008; Liang et al., 2006; Liang et al., 2008) and in the non-autophagic process of endosome maturation (Backer, 2016). ATG14 and UVRAG form a heterodimeric regulatory subcomplex with BECN1 through a parallel coiled coil interaction. One copy of such a regulatory complex then assembles with the catalytic VPS34:VPS15 subcomplex to form the complete PI3KC3 complex. Further variants of complexes I and II are formed in cells by the incorporation of additional subunits, including the C1 activating subunit NRBF2 (Cao et al., 2014; Lu et al., 2014; Zhong et al., 2014) and the potent C2 inhibitor Rubicon (Matsunaga et al., 2009; Zhong et al., 2009).

BECN1 is the smallest subunit in the complex, yet it has a vital and central role as a hub coordinating autophagy with other cell processes, including apoptosis (Hurley and Young, 2017; Levine et al., 2015). BECN1 was the first mammalian autophagy protein to be characterized (Liang et al., 1999), and its discovery as a tumor suppressor connected autophagy to cancer (Liang et al., 1999). BECN1 connects PI3KC3 to the membrane via its C-terminal BARA (beta-alpha repeated, autophagy; the BARA overlaps with region formerly known as ECD) domain (Huang et al., 2012). BECN1 is the target for autophagy regulation by the anti-apoptotic protein Bcl-2 (Pattingre et al., 2005), the C1 complex activating subunit NRBF2 (Young et al., 2016), and phosphoreglation by ULK1 (Egan et al., 2015; Russell et al., 2013), EGFR (Wei et al., 2013), MAPKAPK2/3 (Wei et al., 2015), AMPK (Kim et al., 2013), DAPK (Zalckvar et al., 2009), and Akt (Wang et al., 2012). The Nef protein of HIV-1 has been reported to inhibit autophagy by targeting BECN1 (Kyei et al., 2009). A peptide fragment of BECN1 corresponding to its putative Nef binding site is a remarkably potent inducer of autophagy in cells when cell penetrability is conferred by fusion to the polybasic domain of HIV-1 Tat (Shoji-Kawata et al., 2013). This Tat-BECN1 peptide (T-BP) promotes clearance of toxic protein aggregates and intracellular pathogens from cells (Shoji-Kawata et al., 2013). A major goal of structural studies of autophagic complexes (Hurley and Schulman, 2014) has been to understand how these many regulatory influences on BECN1 are communicated to the VPS34 catalytic domain and converted into changes in PI(3)P levels, thereby regulating autophagy.

PI3KC3-C1 and C2 have essentially the same V-shaped three-dimensional architecture (Baskaran et al., 2014; Rostislavleva et al., 2015). The right arm of the V contains the catalytic domains of VPS15 and VPS34. The V-shaped structure is probably an inactive conformation, as the VPS34 catalytic domain needs to dislodge from its position in this structure to phosphorylate its lipid substrate (Stjepanovic et al., 2017). On its own, the VPS34 catalytic domain has relatively low activity compared to that of the assembled

complex (Stjepanovic et al., 2017). A major role of the rest of the PI3KC3 complex is to deliver VPS34 to membranes. BECN1 seems to play an important role in membrane targeting of the complex. The BECN1-containing subcomplex resides in the left arm of the V, where its parallel coiled-coil binds to the non-catalytic C-terminal helical and WD40 domains of VPS15 and the N-terminal C2 domain of VPS34 (Baskaran et al., 2014; Rostislavleva et al., 2015). BECN1 binds to membrane through its C-terminal BARA domain (Huang et al., 2012; Klionsky and Hurley, 2012), which is located at the end of the left arm together with the BARA-like BARA2 domain of UVRAG. The BECN1 BARA binds to membranes, at least in part, through three hyper-exposed aromatic "finger" residues (Huang et al., 2012; Klionsky and Hurley, 2012) which are located at the outermost tip of the left arm and ideally situated to insert into target membranes.

One of the major endogenous regulatory proteins is Rubicon, which is a widely expressed and potent negative regulator of autophagy. Rubicon tightly associates with PI3KC3-C2 (Matsunaga et al., 2009; Zhong et al., 2009). Rubicon contains an N-terminal RUN domain (RPIP8, UNC-14, NESCA motif), a middle region (MR) that includes predicted disordered, helical, and coiled-coil domains, and C-terminal cysteine-rich (CRD) and Rubicon Homology (RH) domains (Fig. 1A). Rubicon is the founding member of a group of RH-domain containing autophagy and PI3KC3-C2 regulatory proteins, which also includes PLEKHM1 (McEwan et al., 2015; Tabata et al., 2010) and Pacer (Cheng et al., 2017). In this study, we began by seeking to understand how Rubicon inhibits PI3KC3-C2 because of its broad importance in autophagic regulation and for potential insights into the development of autophagy inducers. We discovered that despite Rubicon's C2-directed specificity, it inhibits autophagy by targeting the ability of the BECN1 BARA domain to target membranes. This led us to uncover a mechanism whereby the dynamics of the first β-sheet of BECN1 allow it to unfold and "flip out" of its ground state crystallized conformation and insert into target membranes, promoting VPS34 activity. This mechanism is general to both complexes I and II. It offers an explanation for the potency of the BECN1-derived TBP peptide as an autophagy inducer, and suggests a path forward for the design of small molecule autophagy inducers acting by the same mechanism. Finally, we show that HIV-1 Nef inhibits PI3KC3 by the same mechanism, highlighting the importance of this mode of membrane docking and the wide use of this mechanism to regulate autophagy in normal physiology and infection.

Results

Mapping the Rubicon PIKBD

We began by mapping the PI3KC3-C2 binding and inhibitory region of Rubicon. We found that the RUN and CRD-RH domains did not interact with the intact PI3KC3-C2, despite reported binding of the RUN domain to isolated VPS34 (Sun et al., 2011). The MR bound as well as full length Rubicon, and full binding was retained in a smaller C-terminal fragment of the middle domain (MRC; Fig. 1A). We therefore judged that the MRC encompassed the PI3KC3-C2 binding and inhibitory properties of the full Rubicon protein, and refer to it henceforward as the PIKBD (PI3KC3-C2 binding domain). Both MR and PIKBD formed stable and monodisperse complexes with PI3KC3-C2 on size exclusion chromatography (SEC; Fig. 1B). Full-length Rubicon, MR, and PIKBD all inhibited PI3KC3-C2 lipid kinase

activity in small unilamellar vesicles (SUVs) by a factor of 2 at 12.5 nM concentration (Fig. 1C). We also probed PI3KC3-C2 activity using a giant unilamellar vesicle (GUV) assay in which PI(3)P production is monitored using a GFP-FYVE domain probe and PI3KC3-C2 binding to the membrane is monitored with an mCherry-PI3KC3-C2 fusion (Fig. 1D). Wild-type PI3KC3-C2 robustly generates PI(3)P and binds strongly to the GUV membrane (Fig. 1D). Both full-length Rubicon and the PIKBD essentially completely inhibit both membrane binding and PI(3)P production (Fig. 1D). These data also lead to a second important conclusion, that Rubicon inhibits PI3KC3 by blocking membrane binding.

Rubicon is generally considered to be a specific modulator of PI3KC3-C2 activity. We investigated whether purified full-length Rubicon could bind to recombinant PI3KC3-C1 (Fig. 1E). Only trace binding to PI3KC3-C1 (ATG14) was observed (Fig. 1E). This was in accord with the expectation that binding to complex II would be strongly preferred. The PIKBD mirrored the very weak binding of full-length Rubicon to PI3KC3-C1 (Fig. 1E), indicating that the fragment is, like full-length Rubicon, specific for C2 over C1.

Rubicon PIKBD targets BECN1 BARA β-sheet 1

We used hydrogen-deuterium exchange coupled to mass spectrometry (HDX-MS) to probe Rubicon-PI3KC3-C2 interactions in more detail. HDX of Rubicon-PI3KC3-C2 samples was compared to Rubicon PIKBD and PI3KC3-C2 samples alone at 10, 30, 60, and 90 s (Fig. 2A, B, Fig. S1). No significant (> 5%) changes in protection were seen for VPS34 or VPS15 (data not shown). Two peptides from BECN1 were protected by more than 10 % in the presence of PIKBD, spanning residues 261–287 (Fig. 2A, Fig. S1A, B). These two peptides correspond to the first β sheet of the BECN1 BARA domain (Fig. 2C). Remarkably, the residues spanned by this region (265–287) are nearly identical to those contained in the TBP (residues 267–284) (Shoji-Kawata et al., 2013). Protection of > 5 % was observed in a part of the UVRAG BARA2 (Fig. 2B; Fig. S1C,D) that is adjacent in the three-dimensional structure as inferred from the yeast C2 structure (Fig. 2C) (Rostislavleva et al., 2015).

In order to confirm that β-sheet 1 was the major Rubicon binding site, we first replaced the entire β-sheet 1 with a polar loop (BECN1[BS1PL]), and second, mutated the two most prominent exposed side chains of β-sheet 1, Trp277 and His278 (Fig. 2C), to Asp (BECN1[WH-DD]). BECN1[BS1PL] and BECN1[WH-DD] were expressed as part of reconstituted PI3KC3-C2, and neither was capable of pulling down Rubicon PIKBD (Fig. 2D). In contrast, the BECN1 BARA aromatic finger triple mutation BECN1[DDD], previously shown to block membrane binding (Huang et al., 2012), had no effect on Rubicon binding (Fig. 2D), indicating that the Rubicon binding site does not overlap with the previously established membrane binding site on BECN1. We went on to determine more precisely which portion of PIKBD bound directly to PI3KC3-C2. HDX-MS protection of > 10 % was seen in the first and third of the three predicted helical regions of PIKBD (Fig. 2E, Fig. S2A,B). We determined by pull-down assay that the first helix, which is conserved in the PI3KC3-C2 binding region of Pacer (Cheng et al., 2017), was essential for PI3KC3-C2 binding, while the third region was dispensable (Fig. 2F).

PIKBD inhibits PI(3)P production and autophagy in vivo

To further elucidate the function of PIKBD region of Rubicon, we replaced the central PIKBD residues 488–496 with Ala. We carried out HDX-MS on the mutant construct at three time points and found there was no change to its conformational stability relative to wild-type. We evaluated the impact of overexpressing the wild-type and mutant fragments on PI(3)P generation in cells as detected with a GFP-FYVE probe (Gillooly et al., 2000). Overexpression of Rubicon PIKBD inhibited PI(3)P production as strongly as full length Rubicon, while the PIKBD mutant had minimal effect (Fig. 3A, B). We also examined its effect on autophagic flux in HeLa cells from which Rubicon was genetically deleted. While wild-type Rubicon significantly reversed the autophagic flux in knock out cells, Rubicon PIKBD mutant does not, further highlighting the importance of this region in vivo (Fig. 3C, D). These data show that the inhibitory mechanism observed in vitro and described above is also the mechanism operative in cells.

Cryo-EM structure of PI3KC3-C2 bound to Rubicon PIKBD

An initial negative stain EM characterization of MBP-PIKBD binding to PI3KC3-C2, using the MBP tag as a localization aid, confirmed that PIKBD was situated at the tip of the BECN1-UVRAG portion of the complex. This is at the end of the left arm in the standard view (Fig. 4A). PI3KC3 complexes are conformationally dynamic (Stjepanovic et al., 2017), which has made cryo-EM studies challenging. We generated a fusion between the C-terminus of BECN1 and the PIKBD on the basis of the HDX-MS and negative stain EM studies. The lipid kinase activity of the fusion was identical to that of PIKBD-inhibited PI3KC3-C2 (Fig. S3A). Moreover, this construct manifested the same pattern of HDX protection localized to BECN1 BARA residues 265–287 (Fig. S3B). This fusion was combined with a VPS34-VPS15 fusion (Stjepanovic et al., 2017), previously shown to stabilize the V-shaped "classic" conformation without otherwise perturbing the structure of the subunits. This material led to a sample with improved stability and decreased conformational heterogeneity, which was promising as judged by 2D class averages (Fig. 4B).

A data set was obtained from a VPS34-VPS15:BECN1-PIKBD:UVRAG complex sample on a Titan Krios, leading to a 6.8 Å reconstruction (Fig. 4C, S4–6, Table S1, Movie S1). The most heterogeneous part of the complex is the VPS34 catalytic domain, whose conformational dynamics is reduced, but not eliminated, in the VPS34-VPS15 fusion. This region was therefore removed from averaging by masking. The remainder of the density is generally consistent with the crystal structure of yeast PI3KC3-C2 (Rostislavleva et al., 2015) (Fig. S6). The tip of the N-terminus of the UVRAG coiled coil moves by up to 16 Å, with similar large movements by the associated portion of the BECN1 coiled coil. Further along the coiled coils at their C-terminal ends, UVRAG and BECN1 move by 5 Å and 6 Å, respectively. The UVRAG C2 domain moves by 10 Å. The VPS34 C2 β-sheet core does not move, however, the VPS34 C2 helical insert region moves by up to 10 Å (Fig. S6). These movements likely reflect either the absence of lattice contacts, inherent differences between the human and yeast complexes, or both. These regions are distal to the Rubicon binding site, and these changes are likely unrelated to Rubicon binding and do not affect the interpretation of the Rubicon complex.

The only major additional density feature not accounted for by the four subunits of PI3KC3-C2 was located adjacent to the BECN1 BARA domain (Fig. 4D). The local resolution of this part of the structure is estimated at ~8 Å (Fig. S5B). The main density feature corresponds to a 40 Å long α-helix, which is bound to surfaces formed by the first βαβ repeat of the BARA domain. We provisionally assigned this density to the Rubicon PIKBD. Additional density emanating from the C-terminus of BECN1 was assigned to the BECN1-PIKBD linker. The PIKBD directly contacts Trp277 and His278 (Fig. 2C), consistent with the HDX-MS data.

Based on the orientation of the linker density and the interactions described above, the additional helical density appeared most likely to belong to the first helix α1 of PIKBD. However, at the resolution attained, side chains are not visualized and it is not possible to assign the observed Rubicon density to a unique portion of the PIKBD sequence. Since the PIKBD sequence contains three predicted helical regions (Fig. 1A), we made constructs corresponding to α1 alone and α2-α3 combined. PIKBD-α1 pulled down PI3KC3-C2 effectively, while the α2-α3 did not (Fig. 4E), supporting this assignment. PIKBD-α1 was also inhibited PI3KC3-C2 at 15 nM concentration as judged by the GUV assay (Fig. 4F). However, PIKBD-α1 was somewhat less effective in inhibition than the full PIKBD, suggesting that α2-α3 do contribute to affinity to some degree, even though they are insufficient to pull down PI3KC3-C2 on their own. From these data, we infer that the well-defined helical density modeled as shown in Fig. 4D corresponds to Rubicon α1 and is responsible for inhibiting BECN1.

Membrane docking by BECN1 BARA β-sheet 1

In the crystal structure of BECN1 BARA, 16 residues (248–264) of the BECN1 coiled coil were included in the construct. In the context of this isolated fragment, this region (referred to as "OH" for overlap helix) is folded back on the rest of the BARA domain. In structures of full-length BECN1 in the context of the assembled PI3KC3 (Baskaran et al., 2014; Rostislavleva et al., 2015), however, this region is part of the coiled coil that binds to ATG14 or UVRAG. The position and N-to-C direction of the Rubicon PIKBD allow it to be nearly superimposable with the OH helix (Fig. 5A). This suggests that the face of β-sheet 1 of the BARA domain has a strong propensity to bind to helical structures. The binding of the BECN1 OH to the rest of the BARA domain probably accounts for the conformational stability and crystallizability of the OH-BARA construct (Huang et al., 2012). The HDX-MS data show that the BECN1 BARA β-sheet 1 is relatively dynamic in the full complex in the absence of Rubicon, but are strongly stabilized in its presence. The crystallographic and HDX-MS data taken together strongly suggest that binding of a helix across the face of the β-sheet 1, in particular, strongly stabilizes it in its β-conformation.

The known function of the BECN1 BARA domain is membrane docking (Huang et al., 2012), therefore we hypothesized that PIKBD binding to BECN1 might act by inhibiting the PI3KC3-C2:membrane interaction (Fig. 5B). We tested this idea by carrying out all-atom MD simulations of the BECN1 BARA domain bound to a phospholipid membrane. When β-sheet-1 is locked in its crystallized conformation, the BARA domain binds to the membrane in an upright geometry, the aromatic finger is stably anchored in the membrane, and the finger comprises the primary attachment site (Fig. 5C). When the β-sheet-1 region is

unlocked and allowed to interact with the membrane, Phe270 and 274 form additional stable anchors with the membrane (Fig. 5D, Movie S2), while the positions of surrounding polar residues in the 265–287 region fluctuate. In the unlocked simulation, the geometry remains upright, the aromatic finger remains docked in the membrane, and the fold of the rest of the BARA domain is stable. The main consequence of β-sheet 1 unlocking is to dramatically increase the overall strength of the hydrophobic interactions between the BARA domain and the membrane.

We carried out a series of GUV-based assays to test the docked model illustrated in Fig. 5B-D. The negative control complex containing the aromatic finger mutation BECN1[DDD] failed to bind or generate PI(3)P on 50:50 PI:PS GUVs (Fig. 5E, F), confirming a previous report (Rostislavleva et al., 2015). Consistent with this prediction of the membrane docking model, the BECN1[BS1PL] complex had minimal membrane binding and activity (Fig. 5E, F). We further explored the role of individual BARA β-sheet 1 residues using GUV assays of the hydrophobic anchor residues Phe270 and Phe274, and Rubicon binding residues Trp277 and His278. Phe270 and Phe274 has two roles in the model. They are the major anchors that lodge β-sheet 1 in the BARA domain hydrophobic core, but they are also putative membrane anchors in the extruded, membrane-bound state (Fig. 5D). The double mutant F270S/F274S (BECN1[FF-SS]) essentially eliminates membrane binding and activity (Fig. 5G, H). We tested whether the solvent-exposed residues Trp277 and His278 (Fig. 2C, 5A) might have a dual role in Rubicon binding and membrane anchoring. However, the double mutant BECN1[WH-DD] has essentially wild-type activity (Fig. 5G, H), consistent with the docked structure from the MD simulation. These data highlight the role of the two conserved Phe as the major membrane anchors within β-sheet 1.

BECN1 autophagy-activating peptide promotes PI3KC3 membrane binding in vitro

It is striking that the sequence of β-sheet 1 corresponds almost exactly to the TBP, which potently induces autophagy and upregulates PI(3)P production in cells (Shoji-Kawata et al., 2013). The function of this peptide requires Phe270 and Phe274, both of which are completely buried in the crystal structure of BECN1 BARA (Huang et al., 2012). This leads to a model for an expanded membrane docking site consisting of the three hydrophobic residues of the aromatic finger and additional Phe and other residues from the β-sheet 1 sequence in a flipped-out conformation (Fig. 5B). This model provides a potential explanation for PI3KC3 activation by the peptide, in which the peptide competes with β-sheet 1 for binding to the rest of the BARA domain, so promoting its extrusion and docking onto the membrane.

We tested this hypothesis by conducting SUV and GUV-based activity assays using the TBP peptide. The Tat-containing T-BP construct was used in this experiment even though the cell penetrating ability of the Tat basic residue was not needed in this context. We found that shorter peptides omitting the Tat sequence strongly promoted formation of large PI3KC3-C2 aggregates, precluding further analysis. On the other hand, the basic Tat fusion acted as an anti-aggregating agent. In order to have a low baseline for unstimulated activity and so to avoid saturating the assay, we used liposomes of a composition PC:PE:PI:PS at molar ratio of 60:20:10:10, which is less favorable for PI3KC3 activity. In a SUV-based assay, the

addition of 2.5 to 10 μM T-BP to PI3KC3-C2 increased enzyme activity by 2 to 3-fold (Fig. 6A). Control peptides incorporating F270S/F274S (T-BP[FS]), or with a completely scrambled sequence (T-scrambled), led to no activation (Fig. 6A). We had predicted on the basis of the BECN1-directed nature of T-BP that it should activate both complexes I and II. As expected, a similar activation of PI3KC3-C1 was observed, along with similar behavior by the control peptides (Fig. 6B). The model posits that β-sheet 1 unfolds such that its hydrophobic residues can insert into membranes. This led us to predict that it would not be possible to rescue the inactive BECN1[BS1PL] mutant complex with T-BP. As expected, almost no activity was seen for the BECN1[BS1PL] complex, with or without T-BP (Fig. 6C).

To more directly probe the role of T-BP in promoting membrane binding by PI3KC3, we applied the GUV assay to monitor PI3KC3 membrane binding and PI(3)P production in parallel, using a PC:PE:PI:PS (40:20:20:20) composition. These studies were carried out for 5 min instead of the longer times shown in Fig. 5, as peptide-induced deformations of the GUVs were observed at longer time points. We began with a control condition in which essentially no binding or activity could be observed in this lipid composition. Addition of T-BP potently promoted both GUV membrane binding (red channel) and PI(3)P formation by PI3KC3-C2 (Fig. 6D). It was previously established that PI3KC3-C1 requires high curvature membranes for activity (Fan et al., 2011), and that it is nearly inactive on GUVs (Rostislavleva et al., 2015). Consistent with this past observation, minimal PI3KC3-C1 activity was observed, even in the presence of T-BP (Fig. 6E). This contrasted with the robust activation of PI3KC3-C1 in the presence of high curvature SUVs (Fig. 6B). Remarkably, membrane binding by PI3KC3-C1 was potently promoted by T-BP, despite its lack of enzyme activity. This shows that both PI3KC3-C1 and -C2 are targeted to membranes by the same BECN1 BARA driven mechanism. These data show that it is the enzyme activity, not simply the membrane binding, of PI3KC3-C1 that requires high membrane curvature. Since both complexes contain the same VPS34 catalytic unit, this surprising observation suggests that in the active conformation of PI3KC3, the complex-specific subunits UVRAG and/or ATG14 must interact with the catalytic domain. This point warrants further investigation. The main conclusion of the peptide studies is that all of the predictions of the T-BP activation model shown in Fig. 6F were borne out. T-BP activation acts directly on BECN1, it is dependent on the presence of the anchoring Phe residues in the peptide, it depends on an intact hydrophobic sequence in BECN1 β-sheet 1, it is general for both complexes I and II as expected from its BECN1-directed character, and it is capable of driving the complexes onto membranes even in the absence of enzyme activation.

HIV-1 Nef inhibits PI3KC3-C2 in vitro

Because it had previously been proposed that HIV-1 Nef could inhibit PI3KC3 in autophagy (Kyei et al., 2009) and target BECN1 (Shoji-Kawata et al., 2013), we sought to test whether HIV-1 Nef could inhibit PI3KC3 complexes directly in a purified system. We noticed that the N-terminal region of HIV-1 spanning residues 36–64 had sequence homology with the PIKBD of Rubicon (Fig. 7A). This region of Nef is unstructured in most reports (Geyer et al., 2001), but the most conserved DLEK sequence was observed to have a helical conformation by NMR (Grzesiek et al., 1996). Using SUV assays, we found that at 2.5 to 5 μM concentration, HIV-1 NL4–3 Nef inhibited PI3KC3-C2 by up to two-fold (Fig. 7B).

Consistent with the idea that Rubicon and Nef inhibit by a similar mechanism, we found no inhibition of PI3KC3-C1 (Fig. 7C). Activity on GUVs was barely detectable in the presence of Nef, and membrane binding was almost completely blocked (Fig. 7D, E), consistent with an enzyme inhibition mechanism acting at the stage of membrane docking. Mutation of the DLEK sequence to poly-Ala reversed the ability of Nef to inhibit PI3KC3-C2 on GUVs, confirming that inhibition is mediated by the predicted Nef PIKBD (Fig. 7D, E).

Discussion

In the study, we were able to reach broad conclusions about how BECN1 membrane binding is regulated by studying its inhibition by Rubicon. Rubicon was discovered as an inhibitory subunit of PI3KC3-C2 (Matsunaga et al., 2009; Sun et al., 2010; Sun et al., 2011; Tabata et al., 2010; Zhong et al., 2009). Rubicon is important in its own right as a widely expressed autophagy inhibitor and an exemplar of a larger family of related proteins. Our structural and mutational results show that inhibition and binding are driven strongly by the BECN1 interaction, but also by interactions with UVRAG BARA2. Consistent with this, we replicated in vitro the previous biological observations that Rubicon binds to PI3KC3-C2 much more strongly than -C1. Rubicon is a positive regulator of LC3-associated phagocytosis (Martinez et al., 2015), a pathway whose machinery partially overlaps with that of autophagy. It remains to be seen how the results presented here bear on the role of Rubicon in this distinct pathway. With respect to the generality of the findings beyond Rubicon itself, Pacer also contains a region similar to the critical PIKBD-α1 BECN1 inhibitory region, and this region has been shown to contribute to Pacer's interaction with PI3KC3-C2 (Cheng et al., 2017). We found that HIV-1 Nef also contains such a sequence, and confirmed that HIV-1 Nef directly inhibits PI3KC3-C2, but not PI3KC3-C1, on GUV membranes.

Our observation that T-BP is capable of strongly activating both PI3KC3-C1 and C2 in a purified system establishes a new mechanism for direct BECN1 and PI3KC3 activation, and helps explain why T-BP is such a potent and broad-based activator of autophagy. T-BP has another mode of action in that it binds to an autophagy inhibitor, Golgi-associated plant pathogenesis-related protein 1 (GAPR-1) (Shoji-Kawata et al., 2013), and thereby reverses inhibition by GAPR-1. T-BP induces autophagy more potently than GAPR-1 knockdown in some contexts, however, leading Shoji-Kawata et al. (2013) to propose that other unknown mechanisms likely worked in parallel. Here, we have identified such a mechanism. We found that BECN1 itself is a target of T-BP, that both PI3KC3 complexes are potently activated by T-BP. The BECN1 BARA itself therefore appears to be an attractive target for the creation of novel autophagy inducing agents.

BECN1 is a key node in the autophagic interactome (Levine et al., 2015), yet as the smallest of the three non-catalytic subunits of PI3KC3 complexes, it has not been completely clear why BECN1 evolved to be such an important focal point for autophagy regulation. The results described here highlight the centrality of membrane docking by the BARA domain both as a mechanism for BECN1 to promote PI(3)P formation and autophagy, and as a pivot point for regulation. Binding of the regulators Bcl-2 (Oberstein et al., 2007) and NRBF2 (Ohashi et al., 2016; Young et al., 2016), and phosphoregulation (Russell et al., 2013) of

BECN1, are centered near its N-terminus, remote from its C-terminal BARA domain. While Rubicon, HIV-1 Nef, and T-BP regulate the strength of membrane binding, these other above-mentioned interactors and modifications seem to modulate the strength of the BECN1-VPS34 interaction. These ideas and the data provided here lead to a simple overarching scheme for PI3KC3 regulation by BECN1. N-terminus-directed regulation controls the affinity of the BECN1 subcomplex for the VPS34-VPS15 subcomplex in this scheme, while C-terminus-direct regulation by Rubicon controls the affinity of BECN1 for the membrane.

Here, we showed that several prominent positive and negative modulators of autophagy and PI3KC3 activity, namely Rubicon, HIV-1 Nef, and T-BP, act by directly controlling the ability of PI3KC3 complexes to dock onto membranes via the BECN1 BARA domain (Fig. 7F). While it has been clear for some time that BECN1 is a central node for autophagy regulation, it has been much less clear how BECN1 might actually switch autophagy on and off. The observations here have finally shed light on this question by showing how BECN1 BARA dynamics can be modulated to bring lipid kinase activity above or below baseline, providing a versatile bidirectional regulatory mechanism. This mechanism explains autophagy regulation that is known to occur in normal physiology and in infection, and is harnessed by a potential therapeutic autophagy inducer.

STAR⋆Methods

Contact for Reagent and Resource Sharing

Further information and requests for resources and regents should be directed to and will be fulfilled by the lead contact, James H Hurley (jimhurley@berkeley.edu).

Experimental Model and Subject Details

Cell line—Hela and U2OS cells were grown in DMEM supplemented with 10% FBS, 2 mM glutamine, and antibiotics in a 37°C incubator with a humidified, 5% CO2 atmosphere. The Rubicon KO cell line was generated using CRISPR guide RNAs (5'-cacccgggggtccaagttgccaa –3', and 5'- aaacttggcaacttggacccccg –3') that targets exon 6 in chromosome 3; the common exon of all protein coded splicing variants. Annealed guide RNAs oligonucleotides were inserted into the px458 vector, and the gRNA construct was transfected into HeLa cells using ViaFect™ (Promega) transfection reagent. GFP positive single-cells were sorted into the 96 wells plate by FACS. Candidate single-clone colonies were verified by immunoblotting using anti-Rubicon antibody and Genomic DNA sequence (amplifying primer set; 5'- atatggatccccactggtgacagtgagtgtc –3', and 5'-atatgaattctttcagtctctgcactagcca –3'). The selected Rubicon KO clone had +1 and −7 frameshift indels, and no Rubicon and fragmented gene products bands by immunoblotting

Methods Details

Plasmid construction—Synthetic DNA encoding human RUBCN was cloned into the pCAG vector with an N-terminal MBP tag followed by a tobacco etch virus (TEV) cleavage site. RUBCN truncation constructs and mutants were subcloned into the pCAG vector with MBP tag. Genes encoding PI3KC3 core subunits were cloned into the pCAG vector with an

N-terminal twin-STREP-FLAG tag. BECN1-(GGS)$_4$-RUBCN fusion and BECN1 mutants were subcloned to the pCAG vector with twin-STREP-FLAG tag. For BECN1^{BS1PL} construct, the residues 262–287 of wild type BECN1 were replaced by a polar peptide comprises the amino acid sequence GSDEASEGSGLSSPSALN-SLSSPSAL. DNA encoding UVRAG or ATG14 was cloned into the pCAG vector with an N-terminal GST tag followed by a TEV cleavage site. The GST tag was replaced by mCherry to generate the mCherry tagged UVRAG or ATG14 construct. mStrawberry-Rubicon PIKBD mutant was constructed from mStrawberry-human Rubicon WT (Tabata et al., Mol. Biol. Cell,2010). The amino acids of Rubicon (488 DELKENAHF 496) were replaced by Alanine to make Rubicon PIKBD mutant. All constructs were verified by DNA sequencing.

Protein expression and purification—Protein expression and purification was performed as described previously (Baskaran et al., 2014; Stjepanovic et al., 2017). Transient transfections were performed using polyethylenimine (Polysciences), and cells were harvested after 48 to 72 h expression. Cells were lysed with lysis buffer (50 mM HEPES pH 7.4, 1% Triton X-100, 200 mM NaCl, 1 mM MgCl$_2$, 10% glycerol, and 1mM TCEP) supplemented with EDTA free protease inhibitors (Roche). The lysate was clarified by centrifugation (15000 rpm for 1 h at 4 °C) and incubated with glutathione Sepharose 4B (GE Healthcare) or amylose resin (New England Biolabs) for 2 h at 4 °C, applied to a gravity column, and washed extensively with wash buffer (50 mM HEPES pH 8.0, 200 mM NaCl, 1 mM MgCl$_2$, and 1mM TCEP). The target complexes were eluted with wash buffer containing 50 mM reduced glutathione or 20 mM maltose, and treated with TEV protease at 4 °C overnight. TEV-treated complexes were loaded on a Strep-Tactin Sepharose gravity flow column (IBA, GmbH) at 4 °C. The target complexes were eluted with wash buffer containing 10 mM desthiobiotin (Sigma), and applied to Superose 6 16/50 (GE Healthcare) column equilibrated with gel filtration buffer (20 mM HEPES pH 8.0, 200 mM NaCl, 1 mM MgCl$_2$, and 1 mM TCEP). Peak fractions were collected and used immediately for subsequent assays.

Pull down assay—Transient transfection was performed in 20 mL suspended cells for each condition. Cells were harvested after 48 h expression, and lysed with 2 mL lysis buffer (50 mM HEPES pH 7.4, 1% Triton X-100, 200 mM NaCl, 1 mM MgCl$_2$, 10% glycerol, 1mM TCEP and protease inhibitors). The lysate was clarified by centrifugation (15000 × g for 30 min, at 4 °C) and incubated with 30 μL glutathione Sepharose 4B or amylose resin for 4 h at 4 °C. The protein-bound resin was washed with lysis buffer for 5 times, and then wash buffer (50 mM HEPES pH 8.0, 200 mM NaCl, 1 mM MgCl$_2$, and 1mM TCEP) for 3 times. The proteins were eluted with 100 μL wash buffer containing 50 mM reduced glutathione or 20 mM maltose. The eluted proteins were applied to SDS–PAGE for analysis.

HDX-MS—Amide hydrogen exchange mass spectrometry (HDX-MS) was initiated by a 10-fold dilution of stock wild type and Rubicon fragment associated PI3KC3-C2 complexes (5 μM) into D$_2$O buffer containing 20 mM HEPES (pD 8.0), 200 mM NaCl, 1 mM MgCl$_2$ at 30 °C. Incubations in deuterated buffer were performed for 10 to 90 s. Backbone amide exchange was quenched at 0 °C by the addition of ice-cold quench buffer (400 mM KH$_2$PO$_4$/H$_3$PO$_4$, pH 2.2). Quenched samples were injected onto a chilled HPLC setup with

in-line peptic digestion and desalting steps. Desalted peptides were eluted and directly analyzed by an Orbitrap Discovery mass spectrometer (Thermo Scientific). Initial peptide identification was performed via tandem MS/MS experiments. A Proteome Discoverer 2.1 (Thermo Scientific) search was used for peptide identification. Mass analysis of the peptide centroids was performed using HDExaminer (Sierra Analytics), followed by manual verification of each peptide. The relative deuteron content of the peptic peptides covering PI3KC3-C2 complexes was determined from the centroid of the molecular ion isotope envelope. The average error (n = 3) of all time points and conditions for each HDX experiment was approximately 0.7%.

Lipid kinase assay with small unilamellar vesicles (SUVs)—SUVs were used as the lipid substrate for lipid kinase assay. Briefly, lipid mixture with a molar composition of 60% POPC, 20% POPE, 10% POPS, and 10% POPI or 60% brain PC, 20% brain PE, 10% brain PS, and 10% liver PI was desiccated overnight, resuspended in SUV buffer (20 mM HEPES pH 8.0, 200 mM NaCl), and then sonicated to make a 0.5 mg/ml stock. The lipid kinase assay was carried out using ADP-Glo Kinase Assay (Promega). Freshly purified PI3KC3-C2 and Rubicon associated PI3KC3-C2 complexes were pre-incubated with sonicated SUVs in the reaction buffer (20 mM HEPES pH 8.0, 200 mM NaCl, 1 mM $MnCl_2$, 1mM TCEP). The reaction was initiated by adding $10 \times$ ATP (250 μM), and incubated at room temperature for indicated time. Control reactions without ATP were set up for all proteins. An ATP-depletion reagent was added to terminate the lipid kinase reaction, deplete the remaining ATP, leaving only ADP. Then a kinase detection reagent was added to convert ADP to ATP, which is used in a coupled luciferase reaction. The luminescent output was measured with a GloMax-Multi detection system (Promega) and was correlated with kinase activity.

Giant unilamellar vesicle (GUV) assay—GUVs were prepared as previously described (Wollert et al., 2009). Lipids with different compositions were spread on indium-tin oxide-coated glass slides, and dried overnight in a desiccator. For comparing the activity between different PI3KC3 complexes, lipid mixture with a molar composition of 50% brain PS and 50% liver PI was used. For the BECN1 peptide assay, lipid mixture with molar composition of 40% brain PC, 20 % brain PE, 20% brain PS, and 20% liver PI was used. The lipid film was electro-formed in 400 mM sucrose for 1 h at 60 °C (10 H_Z, 1V). GUVs were then stored at room temperature and used within 48 h. Freshly purified mCherry tagged PI3KC3-C2 complexes and GUVs were incubated in GUV dilution buffer (20 mM HEPES pH 8.0, 190 mM NaCl, 1 mM $MnCl_2$, 1 mM TCEP, 20 μM ATP) at room temperature. A GFP tagged FYVE domain of human Hrs was used as the probe of PI(3)P. The concentration of PI3KC3 was 50 nM, and GFP-FYVE concentration was 7 uM. After 5 min incubation, time-lapse images were acquired in multitracking mode on a Nikon A1 confocal microscope with a 63 × Plan Apochromat 1.4 NA objective. Identical laser power and gain settings were used during the course of all conditions.

Autophagic flux assay—The autophagic flux assay was performed as described previously (Mizushima et al., 2010). Briefly, after twenty-four hours of the transfection with mStrawberry, Rubicon, or Rubicon-mutant to the WT and Rubicon KO cells using

Lipofectamine 2000 reagent (Invitrogen), cells were treated with 125 nM of Bafilomycin A1 (BioViotica, Dransfeld, Germany), a lysosomal inhibitor, for 2 hours in EBSS. Harvested cells were analyzed by the western blotting with anti-LC3 antibody, and the autophagic flux was estimated by the comparison of two samples with or without the inhibitor treatment. The transfection efficacies and loading protein amounts were confirmed by the western blotting with anti-RFP antibody and Ponceau S staining, respectively.

Cell imaging—U2OS cells were starved with EBSS for 2 h after transfection with GFP tagged $2 \times$ FYVE domain of EEA1 and Flag tagged Rubicon, cells were then fixed in 4% formaldehyde for 10 min at room temperature. After washing twice in PBS, cells were incubated in PBS containing 10% FBS and 0.1% saponin to block nonspecific sites of antibody adsorption. The cells were then incubated with appropriate anti-Flag antibody and Alexa Fluor 546 secondary antibody (ThermoFisher) in 0.1% saponin. Confocal images were captured in multitracking mode on a Nikon A1 confocal microscope with a $63 \times$ Plan Apochromat 1.4 NA objective. To quantify the number of GFP-FYVE puncta, a total of 50 cells were recorded and analyzed with Image J.

Negative stain EM sample prep, data collection, and processing—Negatively stained samples of PI3KC3-C2:MBP-Rubicon PIKBD were prepared on continuous carbon grids that had been plasma cleaned in a 10% O_2 atmosphere for 10 s using a Solarus plasma cleaner (Gatan Inc., Pleasanton, CA). Procedures were generally as previously reported (Baskaran et al., 2014; Young et al., 2016). 4 μl of PI3KC3-C2:MBP-Rubicon PIKBD at a concentration of 30 nM in 20 mM Tris, pH 8.0, 200 mM NaCl, 2 mM MgCl2, 1 mM TCEP, and 3% trehalose were placed on the grids and incubated for 30 s. The grids were floated on four successive 40 μl drops of 1% uranyl formate solution incubating for 10s on each drop. The stained grids were blotted to near dryness with a filter paper and air-dried. PI3KC3-C2:MBP-Rubicon PIKBD sample was imaged using an FEI Tecnai 20 electron microscope (FEI, Hillsboro, OR) operated at 120 keV at a nominal magnification of 81,000× (1.5 Å per pixel) equipped with a US4000 CCD camera (Gatan) using a defocus range of −2.5 to −1.0 μm with an electron dose of 35 e–/$Å^2$. Data was collected via Leginon data collection software (Suloway et al., 2005). The power spectrum of each image was estimated with gCTF and particles were picked template-free with Gautomatch. Images were processed in RELION (Kimanius et al., 2016) to generate 2D reference-free classifications.

Cryo-EM sample preparation and data acquisition—Protochips C-flat 2/2 of 400 mesh grids were coated with a carbon support, and glow-discharged in the presence of amylamine for 60 seconds. A sample of PI3KC3-C2 containing the following subunits: VPS15-VPS34 fusion, UVRAG, BECN1–12 residue linker-Rubicon PIKBD fusion was incubated on a grid for 1 minute at 15˚C, 100% humidity. The sample was protected with 0.01% (v/v) NP40 substitute and 1% (w/v) trehalose. The sample was blotted for 3 seconds and then plunge frozen within Mark IV Vitrobot into a 50/50 mix of ethane/propane. The grid was transferred to a FEI Krios microscope operating at 300 kV and collected with a GIF Quantum energy filter (Gatan), and images acquired with a Gatan K2 Direct Electron Detector with a final pixel size of 0.575 Å. Defocus was randomized between −1.3 to −3.3 microns. SerialEM was used to collect an automated dataset of 4,202 micrographs.

Cryo-EM image processing—Individual frames were motion corrected with MotionCor2 (Li et al., 2013) with internal two-fold Fourier binning, discarding the initial two frames, 5 by 5 patch based alignment and dose-weighing up the total exposure of 59.7 electrons/A^2. The contrast transfer function was estimated on the full non-dose weighted micrographs with gCTF version 1.06 (Zhang, 2016). Non-template based picking was performed from non-dose weighted micrographs in Gautomatch, resulting in 388K particles. Particles were extracted in a 352 pixel box, with 8-fold binning and subjected to 2D classification in Relion-2.0 (Kimanius et al., 2016). Following 2D, classes with strong features corresponding to 95K particles were selected and an *ab initio* reconstruction was generated in cryoSPARC (Punjani et al., 2017), resulting in an 8.8 Å map with a Bfactor of −730. The particle angles and reference volume were imported and refined in Relion-2.0 to 8.1 Å and a bfactor of −439. Template-based picking was performed with Gautomatch using seven 2D class averages from Relion-2.0, using the 2D projections from the 8.1 Å reconstruction. The resulting 921,474 particles were extracted and binned by 8, then subjected to 2D classification, cleaning up the data to 622,843 particles. These particles then went through 3D classification, still using bin 8. The resulting 305,942 particles were re-extracted at bin 2, and re-centered. Another round of 3D classification was performed on these 305,942 particles, using a reference map low pass filtered to 60 Å, tau was set 10. The resulting most populated class of 133,007 particles was further refined to 8.6 Å, with a bfactor of −454 $Å^2$. Then, 2D classification without angular sampling was performed, selecting 101,903 particles that were refined to 7.7 Å with a bfactor of −393 $Å^2$. These 101,903 particles were subjected to 3D classification, without angular sampling, with tau set to 16. Two of the three classes were selected, resulting in 72,869 particles, which refined to 7.7 Å and a bfactor of −342 $Å^2$. These 72,869 particles were subjected to another round of 2D classification without angular sampling. A final selection of 42,708 particles were refined to 6.8 Å with a bfactor of −50 $Å^2$.

CryoEM Modeling—A model from a 4.5 Å crystal structure (PDB: 5DFZ) was placed into a 8.6 Å reconstruction using UCSF Chimera using the fit Map in Model tool. In Chimera, model 5DFZ (in Chimera, #0) was split into 6 chains (command: split #0), the nanobody (chain E) and putative N-terminus of Atg6 (chain G) were removed (select #0:.G; delete selected), leaving yAtg6 (hBECN1), yVps38 (hUVRAG), yVps15 (hVPS15), and yVps34 (hVPS34). The models for the kinase domains of yVps34 and yVps15 were then selected and deleted. The remaining models were then fit sequentially within the 8.6 Å EM volume generated in this study (in Chimera, map #1). This volume (map #1) was then colored based on its physical proximity to the now fitted model (#0) and then segmented, *creating a new EM volume. This newly generated reference volume allowed the very flexible VPS34 and VPS15 kinase domains to be excluded from further refinements. This volume was saved and imported into Relion-2.0. When the refinement reached 7.7 Å, an extra helix, possibly accounting for Rubicon PIKBD could be visualized,* the model was then updated to include the human crystal structure of the BECN1 BARA domain, thereby replacing the yAtg6 BARA domain of model 5DFZ. The "OH" (overlap helix) of 4DDP was removed because in the full 4-subunit apo complex, these residues correspond to the C-terminal part of the BECN1 coiled-coil. The OH was replaced with a longer helix of 34 residues corresponding to Rubicon PIKBD. The rest of the model was adjusted, manually, in Coot using real-space

refinement tools, and placement of helices when appropriate. For VPS15, Swiss-modeler was used to replace the yeast model with numbering from human residues. For the C2 VPS34 domain, and BECN1 and UVRAG coiled coils, sequence alignments were used.

Molecular dynamics simulations—The MD simulations of the membrane-attached BECN1 BARA domain started from the crystal structure (PDB id: 4DDP (Huang et al., 2012)). We removed the overlap helix (residues 248–264), used Modeller (Benjamin and Andrej, 2016) to add loop residues 265–268, 387, and 448–450 missing in 4DDP, and capped N- and C-termini by acetylation and amidation, respectively. The structure was protonated at pH 8 using the H++ webserver (http://biophysics.cs.vt.edu) (Anandakrishnan et al., 2012). We placed the protein near a membrane bilayer containing 40% DOPC, 20% DOPE, 20% DOPS, and 20% POPI, as prepared with charmm-gui (http://www.charmm-gui.org) (Jo et al., 2008). The system was solvated with TIP3P water (Jorgensen et al., 1983) and ions (200 mM NaCl). Steepest-descent energy minimization was followed by a short (1 ns) pre-equilibration MD run using the Gromacs molecular dynamics software (vers. 2016.5) (Abraham et al., 2015) using the charmm36 force field for lipids (Klauda et al., 2010) and proteins (Best et al., 2012). All simulations were carried out at 300 K and, if at constant pressure, at 1 bar with semiisotropic pressure coupling. The aromatic finger (residues 359–361) was pulled inside the membrane. All pulling was done in an NVT ensemble at a constant force of 500 kJ mol^{-1} nm^{-1}. Once the aromatic finger was inserted into the membrane, we equilibrated the system in an NPT ensemble for 23 ns, applying soft restraints on the z-positions of the aromatic finger residues. After removing the position restraints, we performed 335 ns of MD simulation in an NPT ensemble using the velocity-rescaling thermostat (Bussi et al., 2007) and the Parrinello-Rahman barostat (Parrinello and Rahman, 1981).

Simulations with unlocked β-sheet 1, residues 265–287 were modeled as a loop using Modeller (Benjamin and Andrej, 2016). Protonation, system preparation, and pre-equilibration followed the preceding protocol. The aromatic finger was pulled into a membrane of the same composition, followed by 30 ns of equilibration. Subsequently, Phe270 and Phe274 were pulled into the membrane with restraints on the z-positions of the anchored aromatic finger. The system was equilibrated in an NPT ensemble for 70 ns with soft z-position restraints on the aromatic finger, and on Phe270 and Phe274. The restraints were then removed and a simulation run was carried out for 242 ns.

Quantification and Statistical Analysis

GUV image quantitation—Data analysis of GUV fluorescence intensities over time was done computationally by a custom developed iPython (Perez and Granger, 2007) code. To mitigate drift of the GUVs, two-channel GUV movies were split into individual channels and frames. Using scikit-image (van der Walt et al., 2014) and OpenCV (Bradski, 2000), for each frame, a thresholding and Hough circle transformation was performed to automatically detect the outline of GUVs and retrieve their individual intensities. Detected GUVs were then matched frame by frame in the same movie to obtain intensity trajectories. Multiple intensity trajectories were calculated from multiple datasets and the average and standard deviation calculated and reported.

Statistical Analysis

The type of statistical test is annotated in the Figure Legends and/or in the Methods segment specific to the analysis. And statistical parameters and significance level are reported in the Figures and/or in the Figure Legends.

Data and Software Availability

The EM density maps have been deposited in the EMDB with accession number 8993. All software and custom scripts are available as detailed in the Key Resources Table. Raw datasets for GUV, unprocessed gel, and western blot images are available at Mendeley datasets (http://dx.doi.org/10.17632/98vgyz7w3z.1).

Supplementary Material

Refer to Web version on PubMed Central for supplementary material.

Acknowledgments

References

Abraham MJ, Murtola T, Schulz R, Páll S, Smith JC, Hess B, and Lindahl E (2015). GROMACS: High performance molecular simulations through multi-level parallelism from laptops to supercomputers. SoftwareX 1–2, 19–25.

Anandakrishnan R, Aguilar B, and Onufriev AV (2012). H++ 3.0: automating pK prediction and the preparation of biomolecular structures for atomistic molecular modeling and simulations. Nucleic Acids Res. 40, W537–W541. [PubMed: 22570416]

Backer JM (2016). The intricate regulation and complex functions of the Class III phosphoinositide 3-kinase Vps34. Biochem. J 473, 2251–2271. [PubMed: 27470591]

Baskaran S, Carlson LA, Stjepanovic G, Young LN, Kim DJ, Grob P, Stanley RE, Nogales E, and Hurley JH (2014). Architecture and Dynamics of the Autophagic Phosphatidylinostol 3-Kinase Complex. eLife 12 9;3. doi: 10.7554/eLife.05115.

Benjamin W, and Andrej S (2016). Comparative Protein Structure Modeling Using MODELLER. Current Protocols in Bioinformatics 54, 5.6.1–5.6.37. [PubMed: 27322406]

Bento CF, Renna M, Ghislat G, Puri C, Ashkenazi A, Vicinanza M, Menzies FM, and Rubinsztein DC (2016). Mammalian Autophagy: How Does It Work? Annu. Rev. Biochem 85, 685–713. [PubMed: 26865532]

Best RB, Zhu X, Shim J, Lopes PEM, Mittal J, Feig M, and MacKerell AD (2012). Optimization of the Additive CHARMM All-Atom Protein Force Field Targeting Improved Sampling of the Backbone phi, psi and Side-Chain chi(1) and chi(2) Dihedral Angles. Journal of Chemical Theory and Computation 8, 3257–3273. [PubMed: 23341755]

Bradski G (2000). The OpenCV library. Dr Dobbs Journal 25, 120–+.

Bussi G, Donadio D, and Parrinello M (2007). Canonical sampling through velocity rescaling. J. Chem. Phys 126.

Cao Y, Wang Y, Saab WFA, Yang F, Pessin JE, and Backer JM (2014). NRBF2 regulates macroautophagy as a component of Vps34 Complex I. Biochem. J 461, 315–322. [PubMed: 24785657]

Cheng X, Ma X, Ding X, Li L, Jiang X, Shen Z, CHen S, Liu W, Gong W, and Sun Q (2017). Pacer mediates the function of class III PI3K and HOPS complexes in autophagosome maturation. Mol. Cell 65, 1029–1043. [PubMed: 28306502]

Egan DF, Chun MG, Vamos M, Zou H, Rong J, Miller CJ, Lou HJ, Raveendra-Panickar D, Yang CC, Sheffler DJ, et al. (2015). Small molecule inhibition of the autophagy kinase ULK1 and identification of ULK1 substrates. Mol. Cell 59, 285–297. [PubMed: 26118643]

Fan W, Nassiri A, and Zhong Q (2011). Autophagosome targeting and membrane curvature sensing by Barkor/Atg14(L). Proc. Natl. Acad. Sci. U. S. A 108, 7769–7774. [PubMed: 21518905]

Galluzzi L, Pedro J, Levine B, Green DR, and Kroemer G (2017). Pharmacological modulation of autophagy: therapeutic potential and persisting obstacles. Nature Reviews Drug Discovery 16, 487–511. [PubMed: 28529316]

Geyer M, Fackler OT, and Peterlin BM (2001). Structure-function relationships in HIV-1 Nef. Embo Reports 2, 580–585. [PubMed: 11463741]

Gillooly DJ, Morrow IC, Lindsay M, Gould R, Bryant NJ, Gaullier JM, Parton RG, and Stenmark H (2000). Localization of phosphatidylinositol 3-phosphate in yeast and mammalian cells. EMBO J. 19, 4577–4588. [PubMed: 10970851]

Grzesiek S, Bax A, Clore G, Gronenborn A, Hu J, Kaufman J, Palmer I, Stahl S, and Wingfield P (1996). The solution structure of HIV-1 Nef reveals an unexpected fold and permits delineation of the binding surface for the SH3 domain of Hck tyrosine protein kinase. Nat Struct Biol 3, 340–345. [PubMed: 8599760]

Huang W, Choi W, Hu W, Mi N, Guo Q, Ma M, Liu M, Tian Y, Lu P, Wang F-L, et al. (2012). Crystal structure and biochemical analyses reveal Beclin 1 as a novel membrane binding protein. Cell Res. 22, 473–489. [PubMed: 22310240]

Hurley JH, and Schulman BA (2014). Atomistic autophagy: the structures of cellular self-digestion. Cell 157, 300–311. [PubMed: 24725401]

Hurley JH, and Young LN (2017). Mechanisms of Autophagy Initiation. Annu. Rev. Biochem 86, 225–244. [PubMed: 28301741]

Itakura E, Kishi C, Inoue K, and Mizushima N (2008). Beclin 1 forms two distinct phosphatidylinositol 3-kinase complexes with mammalian Atg14 and UVRAG. Molecular Biology of the Cell 19, 5360–5372. [PubMed: 18843052]

Itakura E, and Mizushima N (2009). Atg14 and UVRAG: mutually exclusive subunits of mammalian Beclin 1-PI3K complexes. Autophagy 5, 534–536. [PubMed: 19223761]

Jo S, Kim T, Iyer VG, and Im W (2008). Software news and updates - CHARNIM-GUI: A web-based grraphical user interface for CHARMM. J. Comput. Chem 29, 1859–1865. [PubMed: 18351591]

Jorgensen WL, Chandrasekhar J, Madura JD, Impey RW, and Klein ML (1983). Comparison of simple potential functions for simulating liquid water. J. Chem. Phys 79, 926–935.

Kihara A, Noda T, Ishihara N, and Ohsumi Y (2001). Two distinct Vps34 phosphatidylinositol 3-kinase complexes function in autophagy and carboxypeptidase Y sorting in Saccharomyces cerevisiae. J. Cell Biol 152, 519–530. [PubMed: 11157979]

Kim J, Kim YC, Fang C, Russell RC, Kim JH, Fan W, Liu R, Zhong Q, and Guan K-L (2013). Differential Regulation of Distinct Vps34 Complexes by AMPK in Nutrient Stress and Autophagy. Cell 152, 290–303. [PubMed: 23332761]

Kimanius D, Forsberg BO, Scheres SHW, and Lindahl E (2016). Accelerated cryo-EM structure determination with parallelisation using GPUs in RELION-2. Elife 5.

Klauda JB, Venable RM, Freites JA, O'Connor JW, Tobias DJ, Mondragon-Ramirez C, Vorobyov I, MacKerell AD, and Pastor RW (2010). Update of the CHARMM All-Atom Additive Force Field for Lipids: Validation on Six Lipid Types. J. Phys. Chem. B 114, 7830–7843. [PubMed: 20496934]

Klionsky DJ, and Hurley JH (2012). Self-eating with your fingers. Cell Res. 22, 783–785. [PubMed: 22410794]

Kyei GB, Dinkins C, Davis AS, Roberts E, Singh SB, Dong C, Wu L, Kominami E, Ueno T, Yamamoto A, et al. (2009). Autophagy pathway intersects with HIV-1 biosynthesis and regulates viral yields in macrophages. J Cell Biol 186, 255–268. [PubMed: 19635843]

Levine B, Liu R, Dong X, and Zhong Q (2015). Beclin orthologs: integrative hubs of cell signaling, membrane trafficking, and physiology. Trends Cell Biol 25, 533–544. [PubMed: 26071895]

Li XH, He LQ, Che KH, Funderburk SF, Pan LF, Pan NN, Zhang MJ, Yue ZY, and Zhao YX (2012). Imperfect interface of Beclin1 coiled-coil domain regulates homodimer and heterodimer formation with Atg14L and UVRAG. Nature Communications 3, 662.

Li XM, Mooney P, Zheng S, Booth CR, Braunfeld MB, Gubbens S, Agard DA, and Cheng YF (2013). Electron counting and beam-induced motion correction enable near-atomic-resolution single-particle cryo-EM. Nat. Methods 10, 584–590. [PubMed: 23644547]

Liang C, Feng P, Ku B, Dotan I, Canaani D, Oh BH, and Jung JU (2006). Autophagic and tumour suppressor activity of a novel Beclin1-binding protein UVRAG. Nat Cell Biol 8, 688–699. [PubMed: 16799551]

Liang C, Lee JS, Inn KS, Gack MU, Li Q, Roberts EA, Vergne I, Deretic V, Feng P, Akazawa C, et al. (2008). Beclin1-binding UVRAG targets the class C Vps complex to coordinate autophagosome maturation and endocytic trafficking. Nat Cell Biol 10, 776–787. [PubMed: 18552835]

Liang XH, Jackson S, Seaman M, Brown K, Kempkes B, Hibshoosh H, and Levine B (1999). Induction of autophagy and inhibition of tumorigenesis by beclin 1 Nature 402, 672–676. [PubMed: 10604474]

Lu J, He L, Behrends C, Araki M, Araki K, Wang QJ, Catanzaro JM, Friedman SL, Zong W-X, Fiel MI, et al. (2014). NRBF2 regulates autophagy and prevents liver injury by modulating Atg14L-linked phosphatidylinositol-3 kinase III activity. Nature Communications 5, 3920.

Martinez J, Malireddi RK, Lu Q, Cunha LD, Pelletier S, Gingras S, Orchard R, Guan JL, Tan H, Peng J, et al. (2015). Molecular characterization of LC3-associated phagocytosis reveals distinct roles for Rubicon, NOX2 and autophagy proteins. Nat Cell Biol 17, 893–906. [PubMed: 26098576]

Matsunaga K, Saitoh T, Tabata K, Omori H, Satoh T, Kurotori N, Maejima I, Shirahama-Noda K, Ichimura T, Isobe T, et al. (2009). Two Beclin 1-binding proteins, Atg14L and Rubicon, reciprocally regulate autophagy at different stages. Nat.Cell Biol 11, 385–396. [PubMed: 19270696]

McEwan DG, Popovic D, Gubas A, Terawaki S, Suzuki H, Stadel D, Coxon FP, de Stegmann DM, Bhogaraju S, Maddi K, et al. (2015). PLEKHM1 Regulates Autophagosome-Lysosome Fusion through HOPS Complex and LC3/GABARAP Proteins. Mol. Cell 57, 39–54. [PubMed: 25498145]

Mercer TJ, Gubas A, and Tooze SA (2018). A molecular perspective of mammalian autophagosome biogenesis. J. Biol. Chem jbc.R117.810366.

Mizushima N, Levine B, Cuervo AM, and Klionsky DJ (2008). Autophagy fights disease through cellular self-digestion. Nature 451, 1069–1075. [PubMed: 18305538]

Mizushima N, Yoshimori T, and Levine B (2010). Methods in mammalian autophagy. Cell 140, 313–326. [PubMed: 20144757]

Mizushima N, Yoshimori T, and Ohsumi Y (2011). The role of Atg proteins in autophagosome formation. Annu Rev Cell Dev Biol 27, 107–132. [PubMed: 21801009]

Obara K, Sekito T, and Ohsumi Y (2006). Assortment of phosphatidylinositol 3-kinase complexes-Atg14p directs association of complex I to the pre-autophagosomal structure in Saccharomyces cerevisiae. Molecular Biology of the Cell 17, 1527–1539. [PubMed: 16421251]

Oberstein A, Jeffrey PD, and Shi YG (2007). Crystal structure of the Bcl-X-L-beclin 1 peptide complex - Beclin 1 is a novel BH3-only protein. J. Biol. Chem 282, 13123–13132. [PubMed: 17337444]

Ohashi Y, Soler N, Ortegon MG, Zhang L, Kirsten ML, Perisic O, Masson GR, Burke JE, Jakobi AJ, Apostolakis AA, et al. (2016). Characterization of Atg38 and NRBF2, a fifthe subunit of the autophagic Vps34/PIKC3C complex. Autophagy 12, 2129–2144. [PubMed: 27630019]

Parrinello M, and Rahman A (1981). Polymorphic transitions in single crystals- A new molecular-dynamics method. J. Appl. Phys 52, 7182–7190.

Pattingre S, Tassa A, Qu XP, Garuti R, Liang XH, Mizushima N, Packer M, Schneider MD, and Levine B (2005). Bcl-2 antiapoptotic proteins inhibit Beclin 1-dependent autophagy. Cell 122, 927–939. [PubMed: 16179260]

Author Manuscript
Author Manuscript
Author Manuscript
Author Manuscript

Perez F, and Granger BE (2007). IPython: A system for interactive scientific computing. Computing in Science & Engineering 9, 21–29.

Punjani A, Rubinstein JL, Fleet DJ, and Brubaker MA (2017). cryoSPARC: algorithms for rapid unsupervised cryo-EM structure determination. Nat. Methods 14, 290–296. [PubMed: 28165473]

Rostislavleva K, Soler N, Ohashi Y, Zhang LF, Pardon E, Burke JE, Masson GR, Johnson C, Steyaert J, Ktistakis NT, et al. (2015). Structure and flexibility of the endosomal Vps34 complex reveals the basis of its function on membranes. Science 350, doi: 10.1126/science.aac7365.

Russell RC, Tian Y, Yuan HX, Park HW, Chang YY, Kim J, Kim H, Neufeld TP, Dillin A, and Guan KL (2013). ULK1 induces autophagy by phosphorylating Beclin-1 and activating VPS34 lipid kinase. Nat. Cell Biol 15, 741–750. [PubMed: 23685627]

Shoji-Kawata S, Sumpter R, Leveno M, Campbell GR, Zou ZJ, Kinch L, Wilkins AD, Sun QH, Pallauf K, MacDuff D, et al. (2013). Identification of a candidate therapeutic autophagy-inducing peptide. Nature 494, 201–206. [PubMed: 23364696]

Stjepanovic G, Baskaran S, Lin MG, and Hurley JH (2017). VPS34 kinase domain dynamics regulate the autophagic PI 3-kinase complex. Mol. Cell 67, 528–534. [PubMed: 28757208]

Suloway C, Pulokas J, Fellmann D, Cheng A, Guerra F, Quispe J, Stagg S, Potter CS, and Carragher B (2005). Automated molecular microscopy: the new Leginon system. Journal of Structural Biology 151, 41–60. [PubMed: 15890530]

Sun Q, Fan W, Chen K, Ding X, Chen S, and Zhong Q (2008). Identification of Barkor as a mammalian autophagy-specific factor for Beclin 1 and class III phosphatidylinositol 3-kinase. Proc Natl Acad Sci U S A 105, 19211–19216. [PubMed: 19050071]

Sun Q, Westphal W, Wong KN, Tan I, and Zhong Q (2010). Rubicon controls endosome maturation as a Rab7 effector. Proc. Natl. Acad. Sci. U. S. A 107, 19338–19343. [PubMed: 20974968]

Sun Q, Zhang J, Fan WL, Wong KN, Ding XJ, Chen S, and Zhong Q (2011). The RUN Domain of Rubicon Is Important for hVps34 Binding, Lipid Kinase Inhibition, and Autophagy Suppression. J. Biol. Chem 286, 185–191. [PubMed: 21062745]

Tabata K, Matsunaga K, Sakane A, Sasaki T, Noda T, and Yoshimori T (2010). Rubicon and PLEKHM1 Negatively Regulate the Endocytic/Autophagic Pathway via a Novel Rab7-binding Domain. Molecular Biology of the Cell 21, 4162–4172. [PubMed: 20943950]

van der Walt S, Schonberger JL, Nunez-Iglesias J, Boulogne F, Warner JD, Yager N, Gouillart E, Yu T, and Scikit Image C (2014). scikit-image: image processing in Python. Peerj 2.

Wang RC, Wei YJ, An ZY, Zou ZJ, Xiao GH, Bhagat G, White M, Reichelt J, and Levine B (2012). Akt-Mediated Regulation of Autophagy and Tumorigenesis Through Beclin 1 Phosphorylation. Science 338, 956–959. [PubMed: 23112296]

Wei YJ, An ZY, Zou ZJ, Sumpter R, Su MF, Zang X, Sinha S, Gaestel M, and Levine B (2015). The stress-responsive kinases MAPKAPK2/MAPKAPK3 activate starvation-induced autophagy through Beclin 1 phosphorylation. Elife 4, 05289.

Wei YJ, Zou ZJ, Becker N, Anderson M, Sumpter R, Xiao GH, Kinch L, Koduru P, Christudass CS, Veltri RW, et al. (2013). EGFR-Mediated Beclin 1 Phosphorylation in Autophagy Suppression, Tumor tcontaining phosphatidylinositol 3-kinase complex I of autophagy. Proc Natl Acad Sci U S A 113, 8224–8229.

Zalckvar E, Berissi H, Mizrachy L, Idelchuk Y, Koren I, Eisenstein M, Sabanay H, Pinkas-Kramarski R, and Kimchi A (2009). DAP-kinase-mediated phosphorylation on the BH3 domain of beclin 1 promotes dissociation of beclin 1 from Bcl-X-L and induction of autophagy. Embo Reports 10, 285–292. [PubMed: 19180116]

Zhang K (2016). Gctf: Real-time CTF determination and correction. Journal of Structural Biology 193, 1–12. [PubMed: 26592709]

Zhong Y, Morris DH, Jin L, Patel MS, Karunakaran SK, Fu YJ, Matuszak WA, Weiss HL, Chait BT, and Wang QJ (2014). Nrfb2 suppresses Autophagy by Modulating Atg14L-containing Beclin 1-Vps34 Protein Complex Architecture and Reducing Intracellular Phosphatidylinositol-3 Phosphate Levels. J. Biol. Chem 289, 26021–26037. [PubMed: 25086043]

Zhong Y, Wang QJ, Li XT, Yan Y, Backer JM, Chait BT, Heintz N, and Yue ZY (2009). Distinct regulation of autophagic activity by Atg14L and Rubicon associated with Beclin 1-phosphatidylinositol-3-kinase complex. Nat. Cell Biol 11, 468–476. [PubMed: 19270693]

Highlights

Structural mapping of Rubicon binding to PI3KC3-C2

Rubicon stabilizes BECN1 BARA β sheet-1 and blocks membrane docking

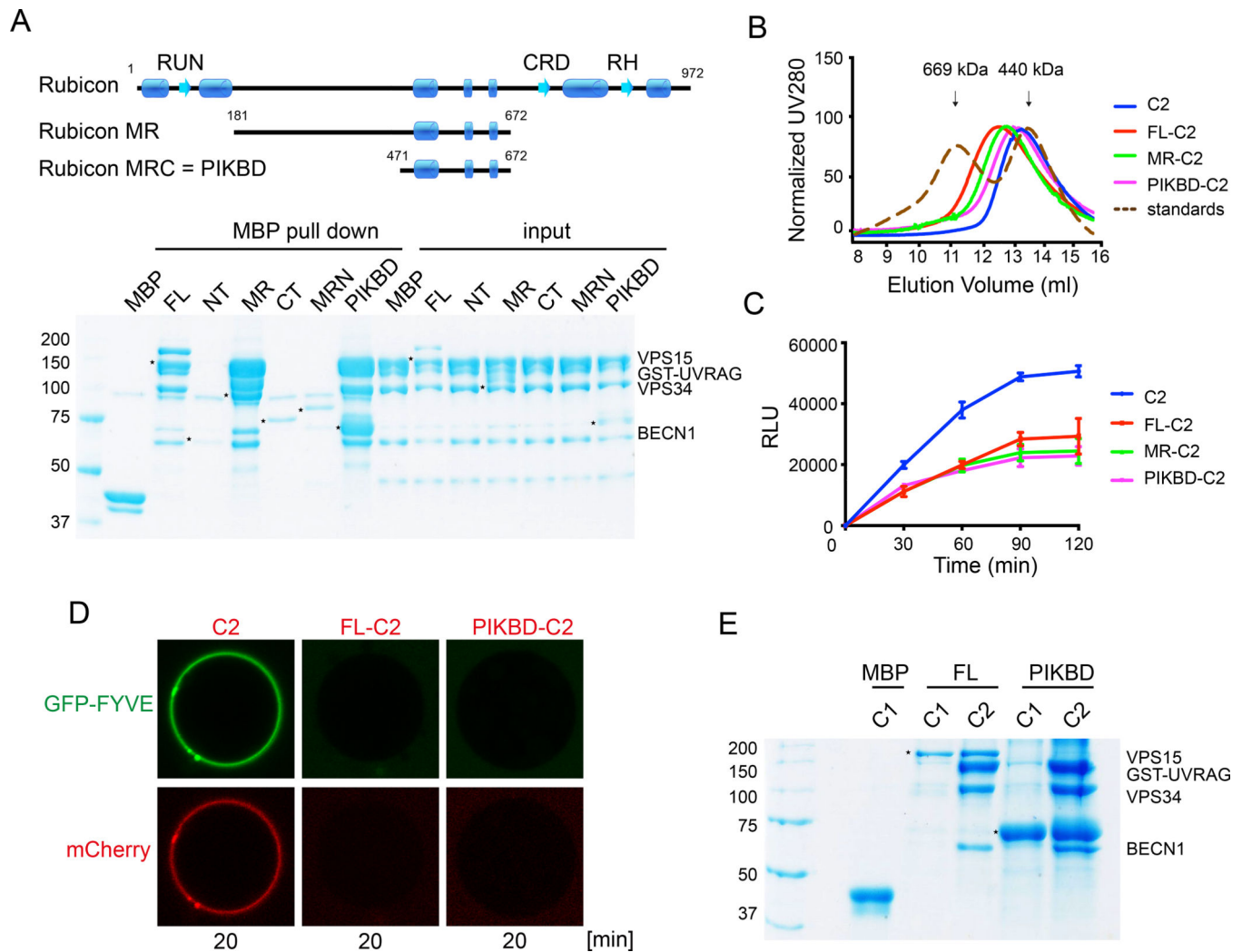BECN1 autophagy-activating peptide promotes BARA membrane binding

HIV-1 Nef modulates PI3KC3-C2 by similar mechanism as Rubicon

Fig. 1. Mapping the Rubicon PIKBD.

(A) Schematic diagram of the predicted secondary structure of Rubicon (upper). MBP tagged full length Rubicon or deletion mutants were co-expressed with the subunits of PI3KC3-C2 (GST tagged UVRAG; Strep tagged VPS34, VPS15 and BECN1) in HEK293 cells. Both MBP and GST pull down were performed. The resulting precipitates were visualized by SDS-PAGE (lower). GST pull-down precipitates were represented as input. FL, full length; MR, middle region; NT, N terminus; CT, C terminus; MRN, middle region N terminus; MRC, middle region C terminus; PIKBD, PI3KC3-binding domain. (B) Size exclusion chromatography of PI3KC3-C2 complexes. Different complexes are indicated with color codes at right. The peak fraction of each complex was used for subsequent activity assays. UV, ultraviolet. (C) Activities of PI3KC3-C2 complexes (12.5 nM) on SUVs containing PI. Different complexes are indicated with color codes. RLU, relative light units. (D) Confocal images of GUVs showing the binding of FYVE domain (green) and different PI3KC3 complexes (red). GUVs were incubated with wild type C2, Rubicon FL-C2, or Rubicon PIKBD-C2 complex respectively. Scale bars, 5 μm. (E) MBP tagged full length

Rubicon or PIKBD were co-expressed with the subunits of PI3KC3-C1 or C2 in HEK293 cells. The MBP pull-down precipitates were visualized by SDS-PAGE.
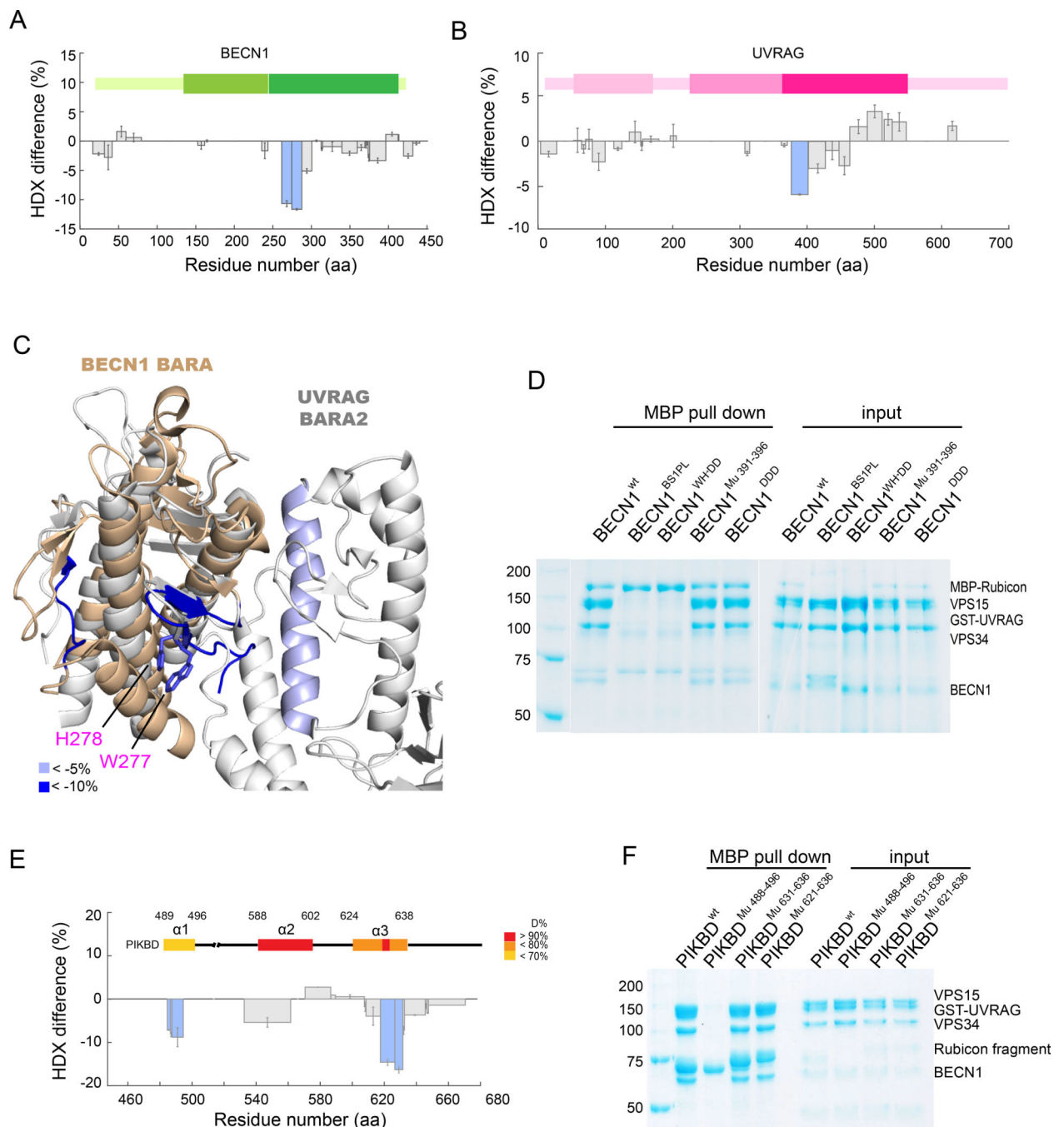
Fig. 2. Mapping binding sites of Rubicon and PI3KC3-C2 by HDX-MS.
(A) Difference plot of percent deuteron incorporation in BECN1 of PI3KC3-C2 versus deuterons incorporated in the presence of Rubicon, 30s in D$_2$O. (B) Difference plot of percent deuteron incorporation of UVRAG of PI3KC3-C2 versus deuterons incorporated in the presence of Rubicon, 30s in D$_2$O. (C) HDX-MS difference map onto the crystal structure of human BECN 1 BARA domain (wheat) and crystal structure of yeast PI3KC3-C2 (grey), BECN1 BARA domain was aligned to the yeast crystal structure. Regions showing a decrease in HDX are depicted in blue (10% decrease) and lavender (5% decrease) in the

presence of Rubicon. (D) BECN1 or mutants were co-expressed with full length MBP-tagged Rubicon and the other subunits of PI3KC3-C2. Both MBP and GST pull-down precipitates were visualized by SDS-PAGE. (E) Difference plot of %D incorporated into Rubicon PIKBD within the PI3KC3-C2 complex versus deuterons incorporated into Rubicon PIKBD alone after 10 s in D_2O. The Rubicon PIKBD secondary structure drawing (upper) illustrates the heat map of apo state. Three predicted α-helices (α1-α3) are colored according to %D exchange. Data are presented as Mean ± Stddev, n=3. (F) MBP tagged Rubicon PIKBD or PIKBD mutants were co-expressed with the subunits of PI3KC3-C2 in HEK293 cells. Both MBP and GST pull-down precipitates were visualized by SDS-PAGE. See also Figure S1 and S2.
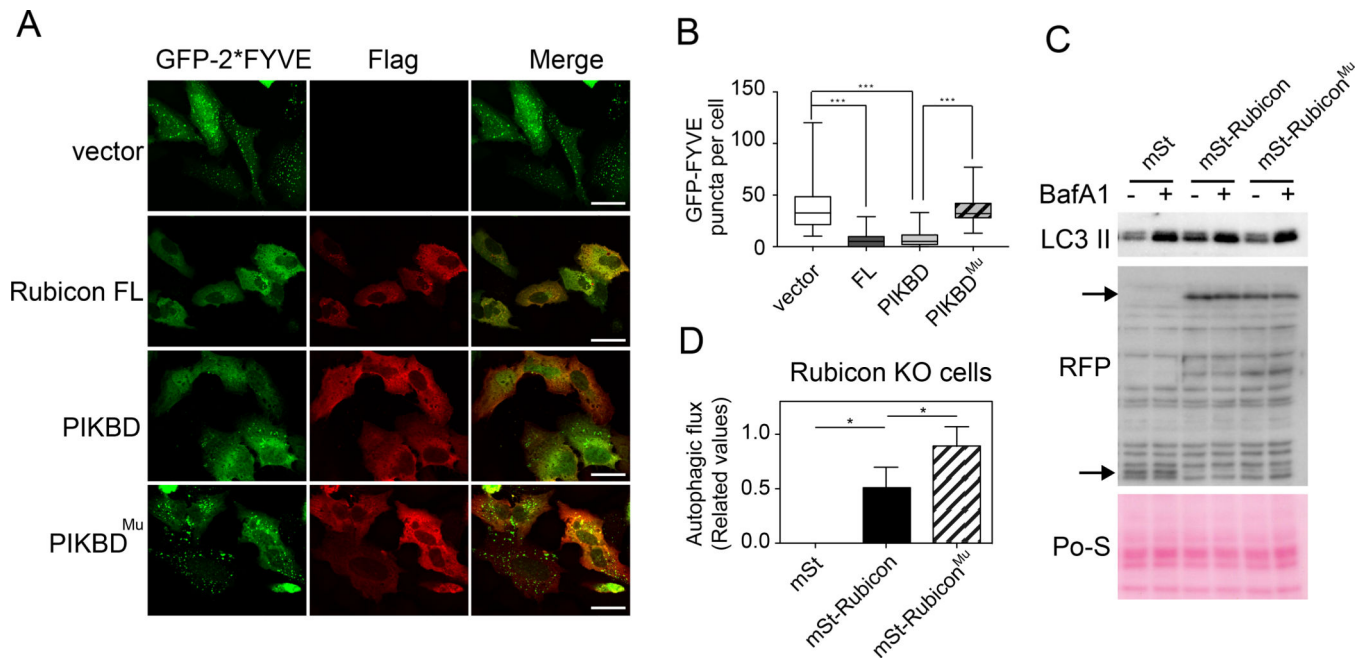
Fig. 3. Rubicon PIKBD inhibits PI(3)P production and autophagic flux in vivo.
(A) Distribution of GFP-FYVE (green) and Rubicon fragment (red) in U2OS cells. Cells
transfected with Flag vector, Flag-Rubicon, Flag-Rubicon-PIKBD, or Flag-Rubicon-PIKBD
mutant were starved with EBSS for 2 h. Scale bars, 10 μm. (B) Quantification of the number
of GFP-FYVE puncta per cell in cells treated as in D. The data are quantified with Image J,
and analyses were performed using GraphPad Prism 5 software. Data are presented as Mean
± Stddev, n = 50. ***p < 0.001. (C) The representative Western Blot for autophagic flux
assay in Rubicon-KO cells with anti-LC3 antibody. After the transfection of mStrawberry
(mSt), mSt-Rubicon, or mSt-Rubicon mutant, cells were starved with EBSS in the presence
or absence of Bafilomycin A1(Baf A1). (D) Quantification of autophagic flux in (C). The
data are quantified using Image J, and analyses were performed using GraphPad Prism 5
software. Comparisons between groups were performed using the one-way analysis of
variance. Data are denoted as Mean ± Stddev, n=3. *p* values　0.05 were considered
significant (*). Anti-RFP antibody and ponceau S (Po-S) were used to confirm the
transfection efficacies of each plasmid and the loading protein amounts, respectively.
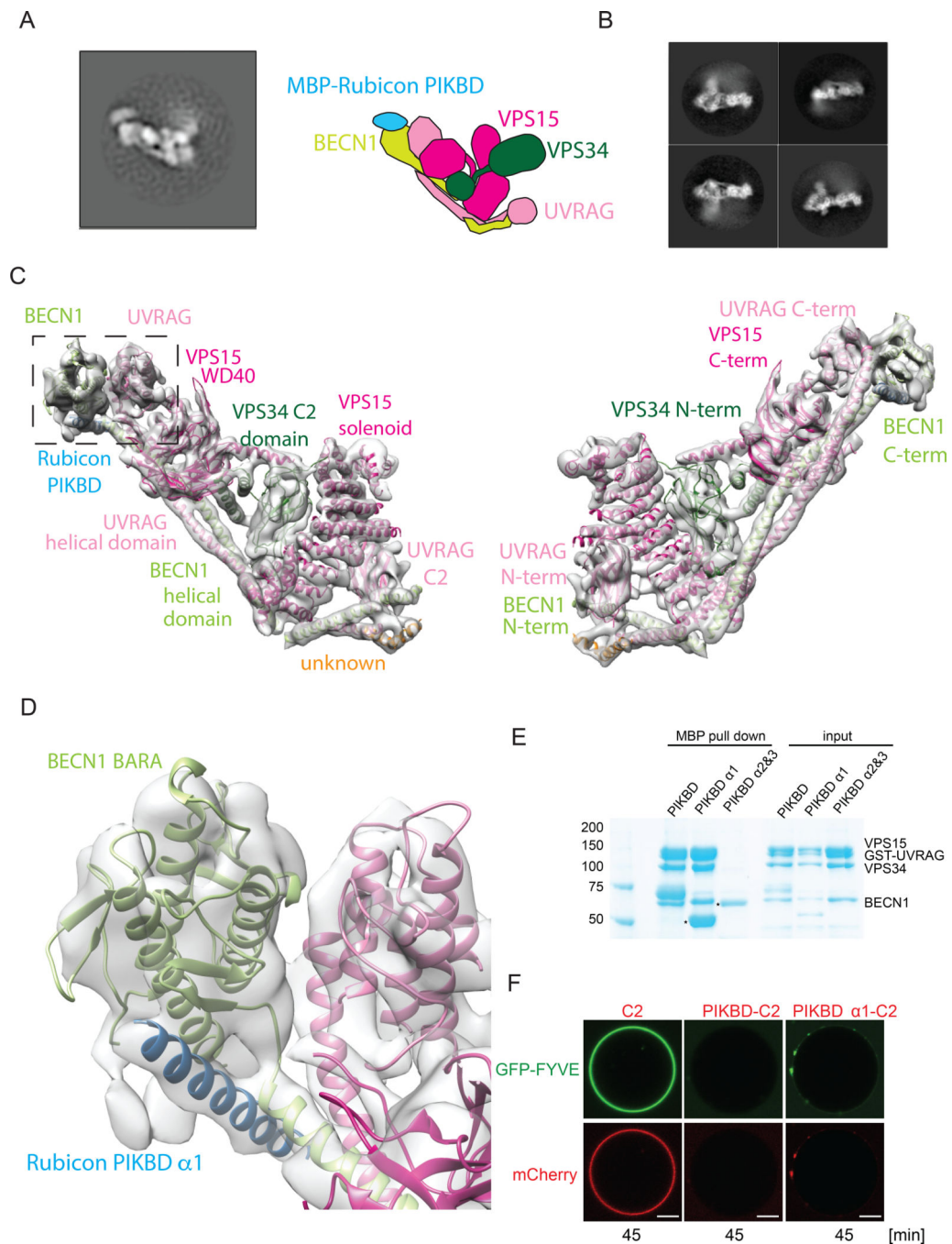
Fig. 4. Cryo-electron microscopy on PI3KC3-C2:Rubicon PIKBD.
(A) Negative stain on PI3KC3-C2 MBP-Rubicon PIKBD and model for domain placement.
(B) 2D-class averages of PI3KC3-C2:MBP-Rubicon PIKBD by cryo-EM. (C) Model fit of
6.8 Å map, BECN1 in lime green, helix corresponding to Rubicon PIKBD, UVRAG in pink,
VPS15 in magenta, and VPS34 in forest green. (D) Inset of the BECN1 BARA domain
where Rubicon PIKBD binds. (E) MBP tagged Rubicon PIKBD α1 or α2&3 were co-
expressed with the subunits of PI3KC3-C2 in HEK293 cells. Both MBP and GST pull-down
precipitates were visualized by SDS-PAGE. (F) Confocal images of GUVs showing the

binding of FYVE domain (green) and different PI3KC3 complexes (red). GUVs were incubated with C2, PIKBD-C2, or PIKBD α1-C2 complex respectively. Scale bars, 5 μm. See also Figure S3-S6, Table S1 and Movie S1.
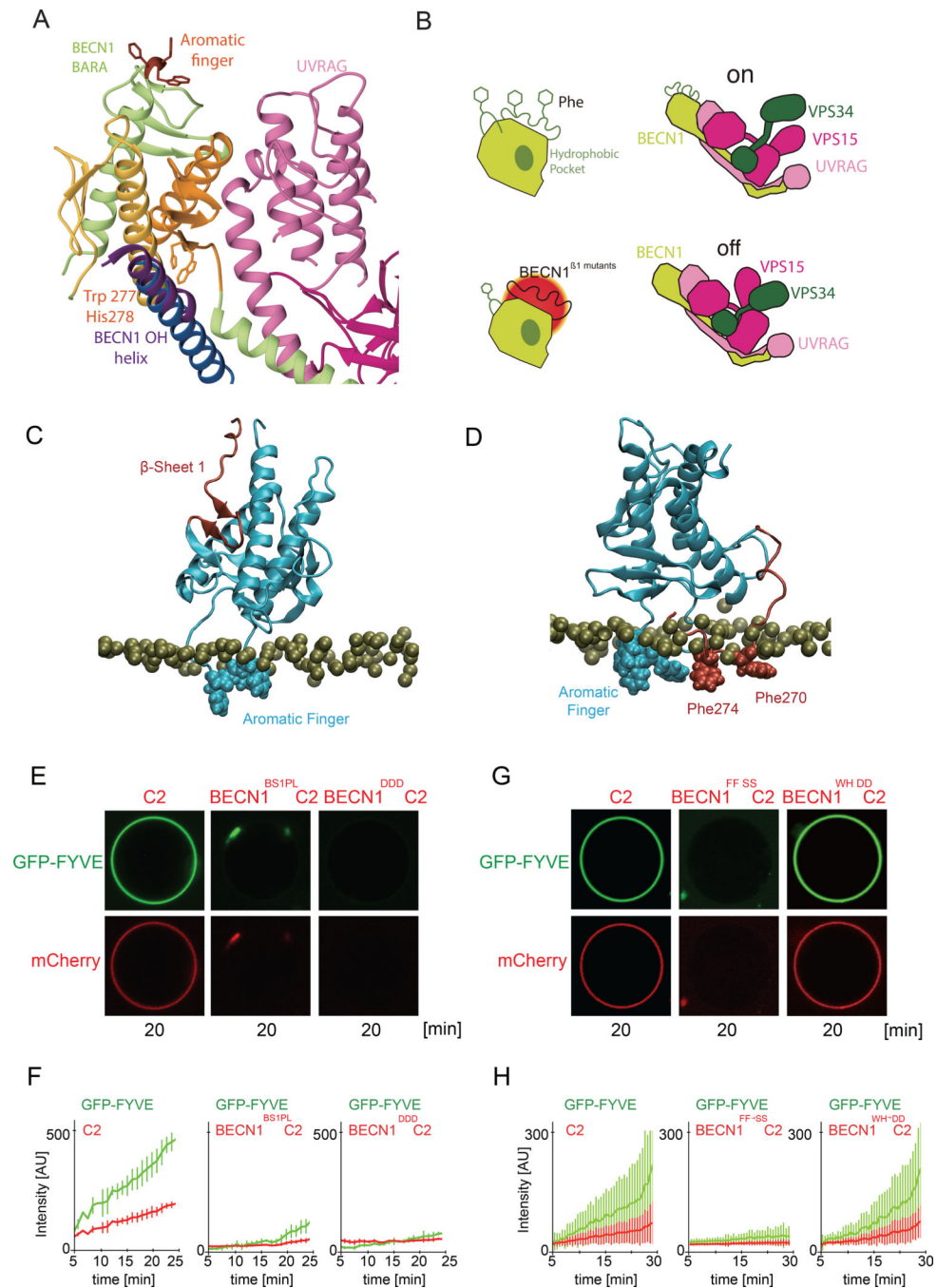
Fig. 5. Membrane docking by BECN1 BARA β-sheet 1.

(A) The OH overlap helix (purple) of BECN1, which is incompatible with the full-length BECN1 subunit, is occupied by a longer helix corresponding to the Rubicon PIKBD (blue). BECN1 BARA domain has three β-α repeats (orange, lime green, and yellow), in the second β-α repeat (lime green) there are three aromatic residues (red) that constitute the aromatic finger necessary for membrane binding. Rubicon-PIKBD (blue) binds to amino acids Trp277 and His278 (orange) located on the first β-α repeat in the BARA domain. Residue register comes from a 1.4 Å crystal structure of the BECN1 BARA domain (4DDP). (B)

Model for membrane docking by BECN1 BARA domain. The BECN1 BARA domain is located at the tip of the regulatory "left hand" arm of the PI3KC3-C2 complex, where it docks onto membranes, promoting access of the kinase to its lipid substrate. One mode of membrane insertion is through the aromatic finger, the second occurs when the β-sheet of the first β-α repeat flips from its hydrophobic pocket in order bind the membrane. Beta sheet 1 mutants are incapable of binding membrane, leading to reduction in PI3KC3 activity. Representative snapshots of MD simulations of membrane-anchored Beclin BARA domain with locked beta-sheet 1 (C) or unlocked beta-sheet 1 (D). BECN1 BARA domain in cyan, locked (C) or unlocked (D) beta-sheet 1 (residues 265–287) in red, phosphate atoms of the upper membrane leaflet depicted as golden spheres. (E) Confocal images of GUVs showing the binding of FYVE domain (green) and different PI3KC3 complexes (red). GUVs were incubated with C2, BECN1^{BS1PL}-C2, or BECN1^{DDD}-C2 complex respectively. (F) Quantitation of the reaction kinetics on the membrane from individual GUV tracing in (C) (see Methods, Mean ± Stddev; C2 N = 13, BECN1^{BS1PL}-C2 N = 7, BECN1^{DDD}-C2 N = 8). (G) Confocal images of GUVs showing the binding of FYVE domain (green) and different PI3KC3 complexes (red). GUVs were incubated with C2, BECN1$^{FF \rightarrow SS}$-C2, or BECN1$^{WH \rightarrow DD}$-C2 complex respectively. (H) Quantitation of the reaction kinetics on the membrane from individual GUV tracing in (G) (Mean ± Stddev; C2 N = 20, BECN1$^{FF \rightarrow SS}$-C2 N = 12, BECN1$^{WH \rightarrow DD}$-C2 N = 20). Scale bars, 5 μm. See also Movie S2.
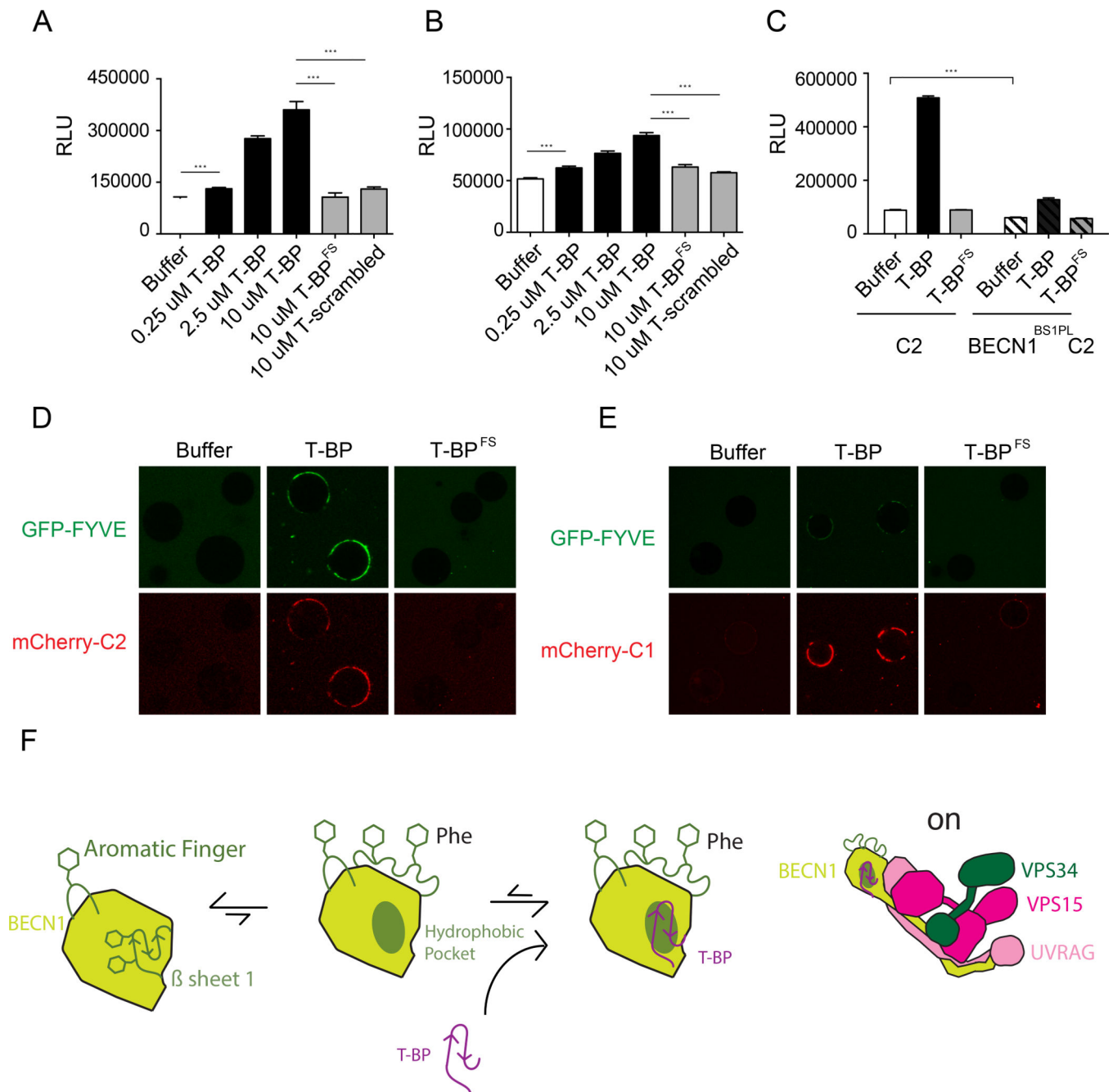
Fig. 6. BECN1 autophagy-activating peptide promotes PI3KC3 membrane binding in vitro.
(A and B) Activities of 25 nM PI3KC3-C2 (A) or PI3KC3-C1 (B) on SUVs in the absence and presence of Tat BECN1 peptide. Data are presented as Mean ± Stddev, n = 3. ***p < 0.001. (C) Activities of 25 nM PI3KC3-C2 or BECN1^{BS1PL}-C2 on SUVs in the absence and presence of Tat BECN1 peptide. Data are presented as Mean ± Stddev, n = 3. ***p < 0.001. (D and E) Confocal images of GUVs showing the binding of FYVE domain (green) and PI3KC3-C2 or PI3KC3-C1 (red) in the absence and presence of BECN1 peptide. Scale bars, 10 μm. (F) Model for PI3KC3 activation by BECN1 peptide. An allosteric switch in beta sheet 1 facilitates this sequence to flip out and bind membranes. This equilibrium favors beta
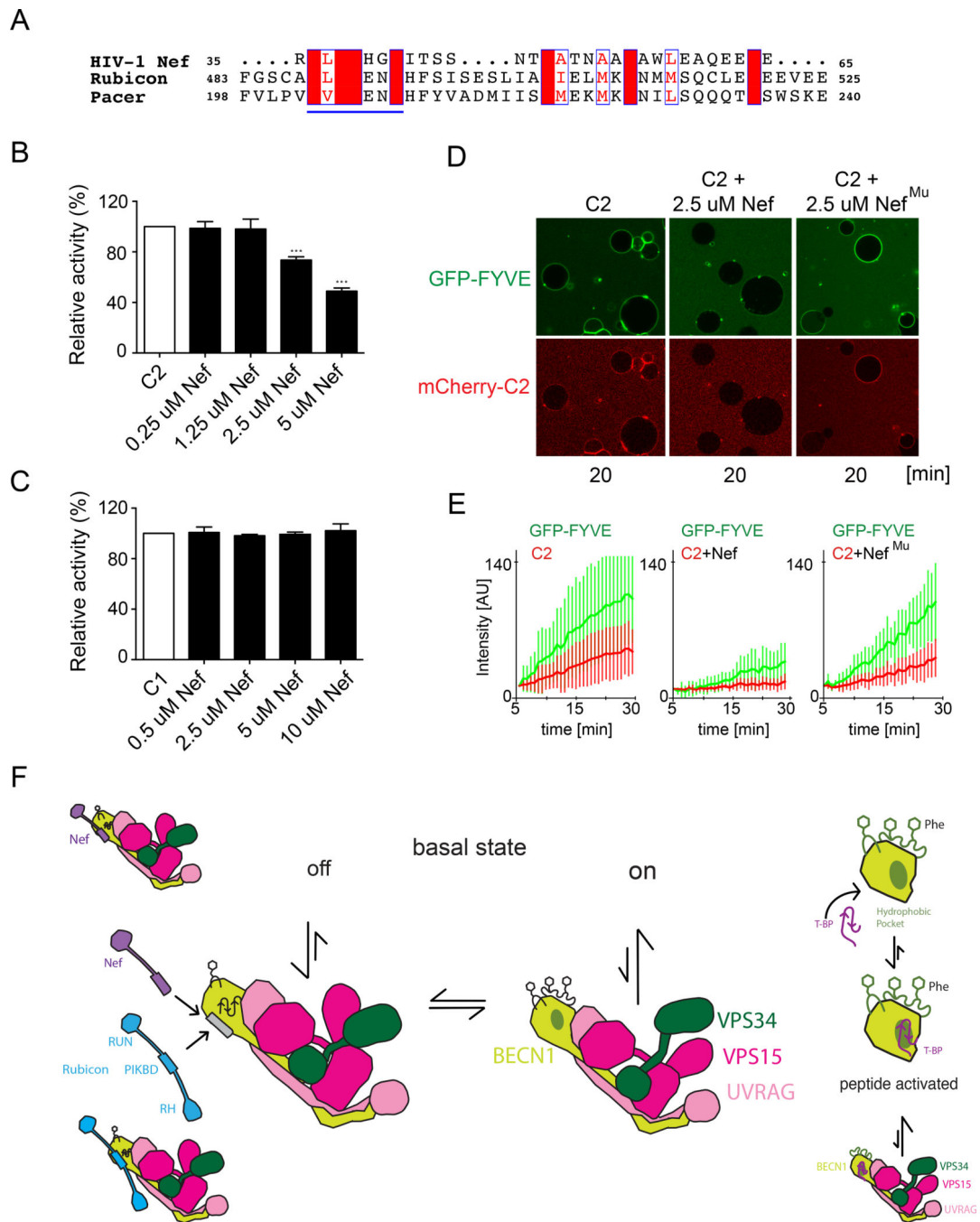
sheet 1 to occupy its hydrophobic pocket over the flipped out state, however, in the presence of T-BP, beta sheet 1 flips out, binds membrane and then activates PI3KC3, as T-BP is present to occupy this hydrophobic pocket.

A

B

C

D

E

F

Fig. 7. HIV-1 Nef inhibits PI3KC3-C2 in vitro.

(A) Sequence alignment for HIV-1 Nef, Rubicon and Pacer. Completely conserved regions among the proteins are colored bright and predominantly conserved regions are enclosed in blue boxes. Residues that were included in the Rubicon mutant that knocked out binding and was used in the cell studies are underlined. (B and C) Activities of 25 nM PI3KC3-C2 (B) or PI3KC3-C1 (C) on SUVs in the absence and presence of HIV-1 Nef. Data are presented as Mean ± Stddev, n = 3. ***p < 0.001. (D) Confocal images of GUVs showing the binding of FYVE domain (green) and PI3KC3-C2 (red) in the presence of wild type Nef and a Nef

mutant in the putative C2 binding site ("Nef^{Mu}", conserved DLEK to AAAA). Scale bars, 10 μm. (E) Quantitation of the reaction kinetics on the membrane from individual GUV tracing in (D) (Mean ± Stddev; C2 N = 12, C2 + Nef N = 7, C2 + Nef^{Mu} N = 8). (F) Schematic for bidirectional regulation of PI3KC3 in normal physiology, infection, and therapeutic intervention.

KEY RESOURCES TABLE

REAGENT or RESOURCE	SOURCE	IDENTIFIER
Antibodies		
Mouse monoclonal anti-Flag M2	Sigma-Aldrich	Cat#1804; RRID: AB_262044
Rabbit polyclonal anti-LC3	MBL International	Cat#PM036; RRID: AB_2274121
Rabbit polyclonal anti-RFP/DsRed	MBL International	Cat#PM005; RRID: AB_591279
Rabbit monoclonal anti-Rubicon	Cell Signaling Technology	Cat# 8465S; RRID:AB_10891617
Chemicals, Peptides, and Recombinant Proteins		
Tat-Beclin1 peptide	UTSW Protein Chemistry Technology Core	N/A
Critical Commercial Assays		
ADP-Glo Max Assay	Promega, Madison, WI	V6930
Deposited Data		
Raw data deposited to Mendeley Data	This paper	http://dx.doi.org/10.17632/98vgyz7w3z.1
Rubicon PIKBD-PI3KC3 C2 Cryo-EM map	This paper	EMBD-8993
Experimental Models: Cell Lines		
HEK GnTI cell line	UC Berkeley tissue culture facility	N/A
U2OS Cell line	UC Berkeley tissue culture facility	N/A
Hela cell line	S. Narumiya (Kyoto University) and T. Hirota (Research Institute of Molecular Pathology)	N/A
Rubicon KO cell line	This paper	N/A
Recombinant DNA		
pCAG-OSF-VPS15	Baskaran et al., 2014	Addgene 99326
pCAG-OSF-VPS34	Baskaran et al., 2014	Addgene 99327
pCAG-OSF-BECN1	Baskaran et al., 2014	Addgene 99328
pLEXm-GST-Atg14	Baskaran et al., 2014	Addgene 99329
pLEXm-mCherry-Atg14	This paper	N/A
pLEXm-GST-UVRAG	Baskaran et al., 2014	N/A
pLEXm-mCherry-UVRAG	This paper	N/A
pCAG-MBP-Rubicon	This paper	N/A
pCAG-MBP-Rubicon NT	This paper	N/A
pCAG-MBP-Rubicon MR	This paper	N/A
pCAG-MBP-Rubicon CT	This paper	N/A
pCAG-MBP-Rubicon PIKBD	This paper	N/A
pCAG-MBP-Rubicon PIKBD^{Mu}	This paper	N/A
mStrawberry-Rubicon	Tabata et al., 2010	N/A
mStrawberry-Rubicon PIKBD^{Mu}	This paper	N/A
pCAG-OSF-BECN1-(GGS)4-Rubicon PIKBD	This paper	N/A
pCAG-OSF-BECN1^{BS1PL}	This paper	N/A
pCAG-OSF-BECN1^{WHDD}	This paper	N/A
pCAG-OSF-BECN1^{FFSS}	This paper	N/A
pCAG-OSF-BECN1^{DDD}	This paper	N/A
His-MBP-Nef	This paper	N/A
His-MBP-Nef^{Mu}	This paper	N/A
pGST2-GFP-FYVE	This paper	N/A
Software and Algorithms		
MotionCor2–1.0.0	Zheng et al., 2017	http://msg.ucsf.edu/em/software/motioncor2.html

REAGENT or RESOURCE	SOURCE	IDENTIFIER
Gct-v1.06	Zhang et al., 2016	https://www.mrc-lmb.cam.ac.uk/kzhang/Gctf/
Relion-2.1	Scheres, 2012	https://github.com/3dem/relion
cryoSPARC-v0.6.5	Punjani et al., 2017	https://cryosparc.com
UCSF Chimera 1.12	Pettersen et al., 2004	https://www.cgl.ucsf.edu/chimera/download.html
Phenix 1.12	Adams et al., 2010	https://www.phenix-online.org/download/
cryoEF	Naydenova and Russo, 2017	https://www.mrc-lmb.cam.ac.uk/crusso/cryoEF/downloads.html
Custom BashEM scripts to (1) monitor data collection and (2) display output files in GNUplot/python	Morris et al., 2018	https://github.com/kylelmorris/localrec_control
Custom python script (Csparc2star- extracts particles from Cryosparc to process in Relion)	From Daniel Asarnow	https://github.com/asarnow
Appion	Lander et al., 2009	http://emg.nysbc.org/redmine/projects/appion/wiki/Appion_Home
Custom Python scripts and Jupyter notebooks	This paper	https://github.com/JohSchoeneberg/GUV_Tracking_Quantification_v2
Proteome Discoverer 2.1	Thermo Fisher Scientific, Waltham, MA	https://www.thermofisher.com/order/catalog/product/OPTON-30795
HDExaminer	Sierra Analytics, Modesto, CA	http://massspec.com/hdexaminer/
Nikon Elements microscope imaging software 4.60	Nikon Corporation, Tokyo, Japan	https://www.nikoninstruments.com/Products/Software/NIS-Elements-Advanced-Research/NIS-Elements-Viewer
Graphpad Prism 7	GraphPad Software, La Jolla, CA	https://www.graphpad.com/scientific-software/prism/
Other		
Glutathione Sepharose 4B GST-tagged protein purification resin	GE healthcare, Chicago, IL	Cat#17075605
Amylose Resin	New England Biolabs, Ipswich, MA	Cat#E8021L
Strep-Tactin Superflow high capacity 50% suspension	IBA Lifesciences, Göttingen, Germany	Cat# 2–1208-010
Superose 6 increase column	GE healthcare, Chicago, IL	Cat#29091596